

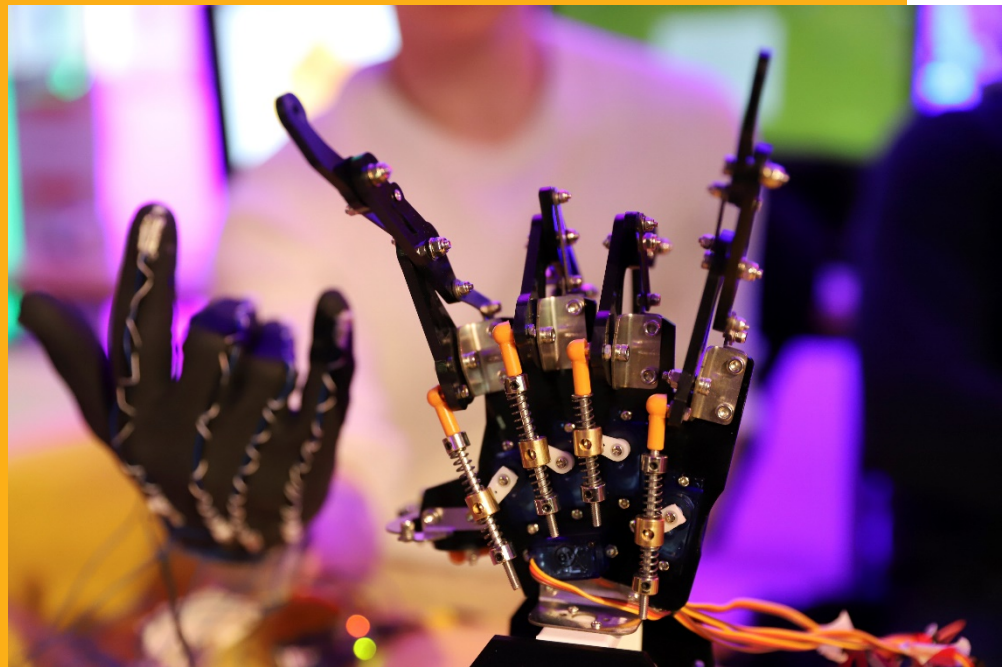
Mechanical Engineering

Proceedings of the 4th Baltic Mechatronics Symposium

Tallinn April 25, 2019



Kiviluoma Panu
Kuosmanen Petri
Otto Tauno



Proceedings of the 4th Baltic Mechatronics Symposium

Tallinn April 25, 2019

Kiviluoma Panu
Kuosmanen Petri
Otto Tauno

Abstract

Aalto University, P.O. Box 11000, FI-00076 Aalto www.aalto.fi
TALTECH, Ehitajate tee 5, 19086 Tallinn, Estonia www.ttu.ee

Author

Kiviluoma Panu, Kuosmanen Petri, Otto Tauno

Name of the publication

Proceedings of the 4th Baltic Mechatronics Symposium

Publisher Aalto University School of Engineering

Unit Mechanical Engineering

Field of research Mechanical Engineering

Language English

Abstract

The Baltic Mechatronics Symposium is annual symposium with the objective to provide a forum for young scientists from Baltic countries to exchange knowledge, experience, results and information in large variety of fields in mechatronics. The symposium was organized in co-operation with Taltech and Aalto University. The venue of the symposium was Nordic Hotel Forum Tallinn. The symposium was organized parallel to the 12th International DAAAM Baltic Conference and 27th International Baltic Conference BALTMATTRIB 2019. The selected papers are published in Proceedings of Estonian Academy of Sciences indexed in ISI Web of Science.

The content of the proceedings

1. Continuous wet spinning of cellulose nanofibrils
2. Development of motor efficiency test setup for direct driven hydraulic actuator
3. Development of pressure former for continuous nanopaper manufacturing
4. Device for tree volume measurements
5. Effect of external load on rotor vibration
6. Granular jamming based gripper for heavy objects
7. Integrated car camera system for monitoring inner cabin and outer traffic
8. Inverted pendulum controlled with CNC control system
9. Multi-material mixer and extruder for 3D printing
10. Object detection and trajectory planning using a LIDAR for an automated overhead crane

Keywords Mechatronics, Industrial Internet, Sensors, Actuators, Control

ISBN (pdf) 978-952-60-3781-3

Location of publisher Helsinki

Pages 63

Continuous wet spinning of cellulose nanofibrils

Niko Lappalainen^{1,a}, Juho Piilola^{1,b}, Antti Romo^{1,c}, Ling Wang^{2,d}, Ville Klar^{1,e}
Panu Kiviluoma^{1,f} and Petri Kuosmanen^{1,g}

¹Department of Mechanical Engineering, Aalto University, Finland

²Department of Bioproducts and Biosystems, Aalto University, Finland

^aniko.m.lappalainen@aalto.fi, ^bjuho.piilola@aalto.fi, ^cantti.romo@aalto.fi, ^dling.wang@aalto.fi,

^eville.klar@aalto.fi, ^fpanu.kiviluoma@aalto.fi, ^gpetri.kuosmanen@aalto.fi

Keywords: Nanocellulose, biomaterial, cellulose nanofibrils, wet spinning

Abstract

New nanocellulose based materials have drawn much attention due to their great properties with low environmental impact. Cellulose nanofibrils (CNFs) have mechanical properties comparable to carbon fiber and steel, which can be enhanced by drawing during wet spinning of CNF. Grand challenges in nanocellulose processing have been identified that limit the potential for expanding nanocellulose usage in new composite materials. In this paper we present a prototype of a wet spinning line that uses dual bath -approach to produce coagulated and washed CNF filament that enables further research of wet spinning of CNF. This prototype enables easy control of crucial parameters involved in CNF wet spinning and it can be used with new, optimized parameters derived from future research. In this paper, we also identify an issue regarding CNF creeping that should be addressed in future research.

Introduction

The environmental issues regarding plastics such as carbon emissions and microplastics ending up in the ocean have pushed material research towards bio-based options [1, 2]. Also, the consumers, industry and governments are increasingly demanding for products that are made from renewable resources with low environmental impact [3].

A promising substitutive material is nanocellulose, also referred to as cellulose nanoparticles (CNs), obtained from lignocellulosic biomass [3, 4]. Nanocelluloses can be categorized in three groups; bacterial nanocellulose (BNC), nanocrystalline cellulose (NCC) and cellulose nanofibrils (CNF), although there exist many synonyms for these groups of nanocelluloses. Each of these groups of nanocelluloses possess different kind of properties [5]. Cellulose nanofibrils (CNF) are lightweight, biodegradable and their stiffness is comparable to Kevlar and steel [4, 6]. Nanocelluloses are ideal materials for composite products and their potential applications include flexible displays, polymer fillers, biomedical implants, fibers and textiles, and many others [3].

Continuous fibers of nanocellulose with a desired length can be formed by various spinning techniques, such as dry-spinning, wet spinning or dry-jet wet spinning. The only techniques applied to CNF spinning without added polymers are wet and dry-spinning. [6] Mechanical properties of man-made cellulosic materials depend on the cellulose crystallite alignment, which can be enhanced by drawing during the spinning. However, this can be difficult to implement in CNF spinning because of the low aspect ratio of CNF. [6, 7, 8]

Four grand challenges in nanocellulose processing have been identified that, when solved, would greatly increase the potential for expanding nanocellulose usage in new composite materials. These challenges are: 1) decreasing the internal damage in CNs as a result of the extraction process, 2) narrow the particle size range for a given CN processing methodology, 3) decrease the cost of the extraction process and 4) scaling up production to industrial quantities. [3]

In this paper, we focus on the challenge of scaling up production of CNF, which is challenging especially if controlled structure and characteristics of the material are demanded [6] and we present a development tool for exploring nanocellulose wet spinning that enables further research of CNF and wet spinning of CNF and could later allow the production to be scaled up to industrial quantities.

Methods

In this paper, we present a prototype, that could enable more reliable manufacturing of CNF filaments, also allowing the manufacturing of longer filaments. This prototype can be used to explore nanocellulose wet spinning further.

The wet spinning process used in this study is a dual bath -approach (Fig. 1) where the CNF suspension is pumped to a coagulation bath containing anti-solvent, through a small diameter spinneret. In the coagulation bath, the CNF will solidify and after solidification the CNF filament is transferred to a washing bath where the filament is washed from the salt solution of the coagulation bath. After the washing, the filament is transferred from the washing bath so that the filament could be dried and spooled.

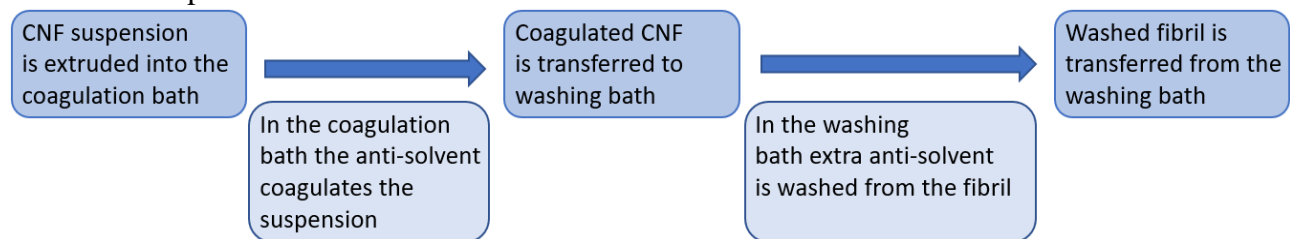


Figure 1. Dual bath -approach used for the CNF suspension.

Following requirements were set for the new spinning line setup:

- Include one solidification bath, where the CNF suspension could be extruded, and it would coagulate in that bath.
- Include one washing bath and a way to transfer the fragile CNF filaments from coagulation bath into washing bath without breaking.
- Support operation with Nexus 3000 or 6000 syringe pump.
- Modular structure, meaning that the bath lengths and roller diameters should be changeable, and the line should support adding a drying and spooling section after the baths.
- Fit in the 190x70cm fume cupboard.
- Adjustable speed of the filament at each roller.
- Simple and small user interface to enable the control of the spinning line. The operation should be possible when wearing lab equipment.

The build can be divided in mechanical structure and control system for further examination of the prototype.

Mechanical structure. The prototype was required to have a maximum dimensions of 190x70cm. This was required, because in the future, the anti-solvent in the solidification bath may be switched into acid that would require the setup to be in a fume cupboard. The frame of our prototype was built from aluminum profile and as for the baths, stainless steel Gastronorm sized catering containers were used to eliminate the need for custom part manufacturing in case of later development of our prototype. The prototype has three 42.4 mm diameter rollers in total, which were all knurled to reduce the agglutination of the filaments into the rollers. The attachments for the rolls were all made identical and they can be used to wet spin filaments in different roller sizes ranging from 33.7 mm to 88.9 mm in diameter. All parts of the roller holders that have a possibility of touching the solidification bath's liquid were made from acid proof stainless steel or polytetrafluoroethylene (PTFE). Even though that

was not necessary with current salt solution, this enables further development of various anti-solvents with this prototype. In addition, a holder was manufactured to hold the spinneret steady while operation and exhaust valves were inserted to the baths to allow easy and safe evacuation of the liquids in the baths. Picture of the prototype is presented in Fig. 2.

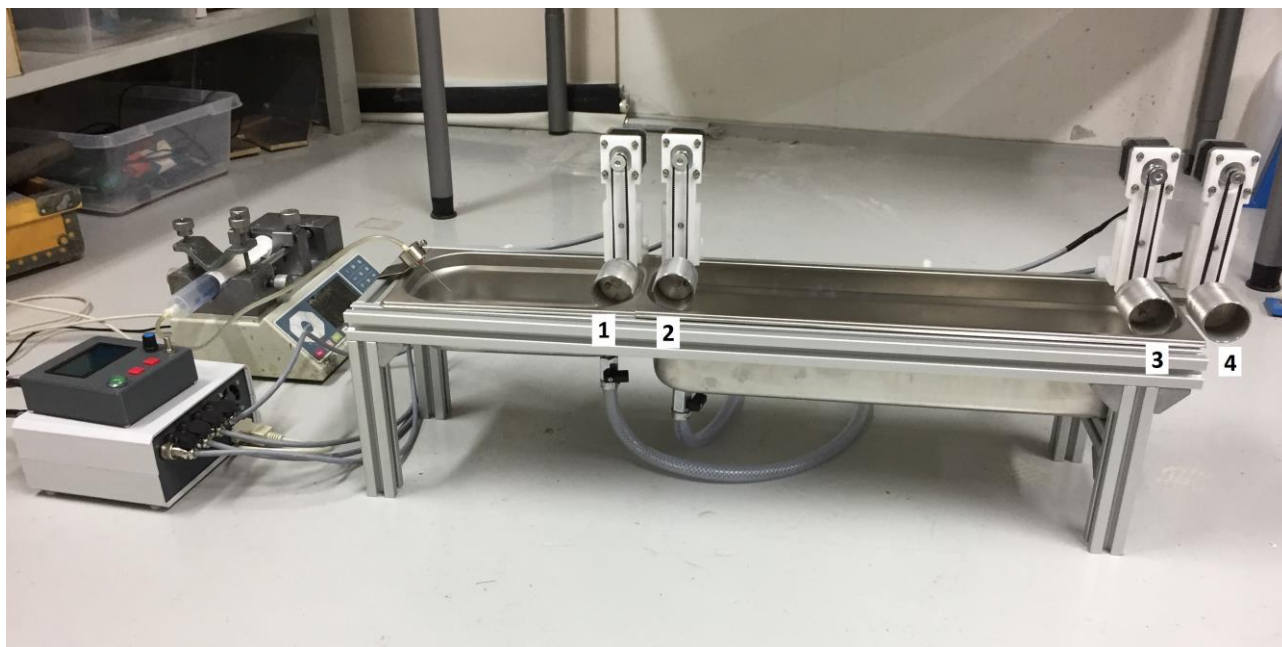


Figure 2. Prototype used in this study, rollers numbered from 1 to 4, where roller 1 is the first one after extrusion.

Control. 1.5 A NEMA 17 Stepper motors were used to enable steady speed control of each roller. To achieve more seamless rotation and speed control, each motor was run in 1/8 stepping mode. An open-loop controller was built for the motors using Arduino Mega and A4988 drivers. Non-feedback control was used, since the forces and speeds in this setup were estimated to be relatively low, and therefore a reliable operation without any step skipping was achieved by only setting the currents on a sufficient level from the drivers. A RAMPS 1.4 shield was used on top of the Arduino, providing readymade slots for five stepper drivers, of which one slot had readymade pins for two motors and the rest had pins for one motor each. Therefore, a total of six motors with five independent speeds could be controlled with this setup. The RAMPS board also supports attachment of Full Graphic Smart Controller including LCD, a beeper and relative rotary encoder, and therefore this was used as the base for the user interface. One on/off switch and a precision potentiometer were added beneath the Full Graphic Smart Controller to enable overall control of the line speed. The Arduino is connected to the Nexus 3000 pump with a RS232, 9 pin serial connection, which is used for sending commands to the syringe pump from the Arduino to control the volumetric speed and state (pump on, pump off) of the syringe pump through the user interface of the spinning line setup. The schematics of the whole control system is visualized in Fig. 3.

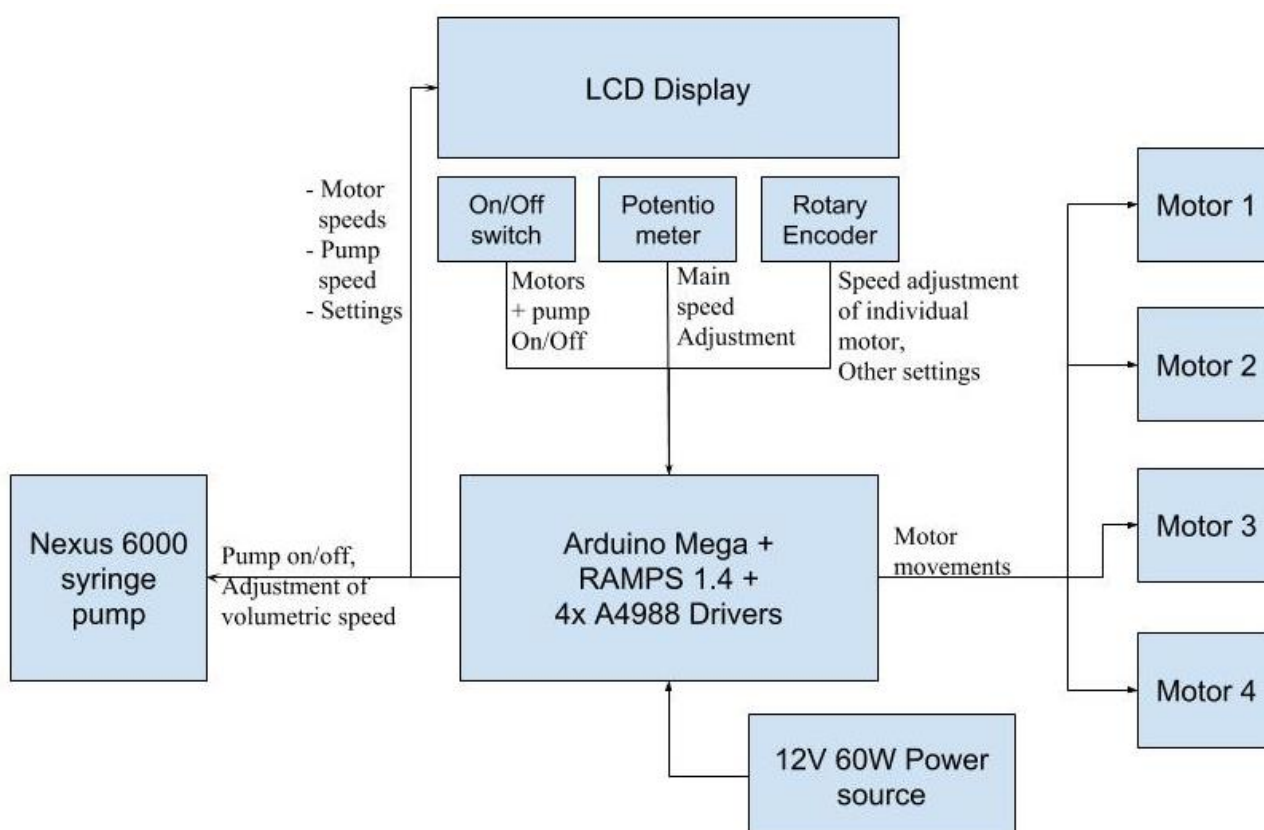


Figure 3. Schematics of the control system used in the prototype.

Testing conditions. The process used in this study is conducted in room temperature and salt solution is used in the coagulation bath. The aqueous CNF suspension is pumped into the salt solution and a set of two rolls is used to transfer the CNF from solidification bath into the washing bath without breaking. Third roll is used at the end of the washing bath to allow the CNF transported into fourth roller and the fourth roller is used as a collector to collect all washed filaments onto a single roll. This fourth roller can later be utilized to assist in the transfer of the filaments from the washing bath into drying or spooling. The rotating speed of all rolls is interrelated to the extrusion speed of the spinneret and drawing speed between every roller is adjustable.

The testing was done with CNF suspension extrusion speed of 1 ml/min from a 1.2 mm diameter spinneret, and without any drawing between extrusion and washing, as well as without drawing during the washing. The operation reliability of the machine was evaluated by means of the length of filament without interruptions.

Results

The testing was conducted with roller locations above water and a gap of 50 mm between rollers 1 and 2, as well as rollers 3 and 4. Testing was done without any drawing, meaning that the circumferential velocity of all rollers were adjusted to match the extrusion speed of the CNF suspension to the coagulation bath. During testing we found that when there was no draw added between rollers 1 and 2, the CNF filament stretched between these two rollers and resulted in the filament eventually touching the frame and breaking. By lifting roller 1 eight mm higher than roller 2 and adding a draw of 3% to roller 2 we managed to eliminate this stretching and the filament's transition between these two rollers became smooth. This creeping effect did not occur during the transition between the last two rollers, hence there was no draw added between rollers 3 and 4.

In the beginning of the operation, the filament had to be manually guided from the solidification bath into the first two rollers, as well as from the washing bath into the last two rollers. But after

guiding the filament once through the whole setup, the spinning required no more manual operating, as the filament was automatically extruded, guided through the setup and finally spooled on the fourth roller. Without any drawing in baths and just 3% drawing between rollers 1 and 2, the prototype succeeded in the test and resulted in continuous spinning of the CNF, where the washed filament was collected in the fourth roller (Fig. 4). The amount of CNF suspension in the syringe pump was the limiting factor to the amount of washed filament.



Figure 4. During testing, the washed filament was collected in the fourth roller (right-hand roller in the picture).

Based on our test, this prototype enables the major parameters regarding wet spinning to be easily adjusted. This includes the extrusion speed of the CNF, altering the locations of each roll and changing the speed of each roll, which results in an easy control of drawing ratios in every step of the operation.

Discussion

In this study, we presented a prototype of a development tool that allows further studying of cellulose nanofibrils, wet spinning of cellulose nanofibrils and continuous wet spinning line. This prototype includes a coagulation bath, filled with salt solution and a washing bath filled with water. The prototype enables communicating with Nexus 3000 and 6000 syringe pumps and it has four, individually adjustable rollers to navigate the CNF between and out of these baths.

Due to the increasing demand for products made from renewable sources and with low environmental impact, development of manufacturing CNF filaments is researched widely, and these studies may result in better optimized wet spinning parameters. Future optimization of CNF filament manufacturing may result in different extrusion and drawing speeds, bath lengths or bath liquids than what were used in this study. But this study shows that due to this prototype's ability to easily alter roller sizes, locations and speeds this prototype is able to respond to the changes in crucial parameters involved in CNF wet spinning and can be used to research wet spinning of CNF further.

In this study, we identified an issue regarding nanocellulose creeping that should be addressed in further research. Between different transitions, the filament is hanging on air, which results in a downward gravitational force that could affect the cellulose crystallite alignment in the fiber and its mechanical properties. Further research should address how this affects the properties of CNF and how different drawing ratios during transitions affect these properties.

Further research should also address the type of drying and spooling to be used after coagulation and washing of the filament, as well as optimal drawing ratios for rollers in coagulation and washing stages. The prototype presented in this study, does not eliminate any specific drying or spooling mechanisms, and due to the fourth roller used at the end of the line, this prototype can be extended to include various types of drying and spooling after the washing bath.

References

- [1] S. Wright, R. Thompson, T. Galloway. The physical impacts of microplastics on marine organisms: a review, *Environmental Pollution*. 178 (2013) 483–492.
- [2] J. Allwood, J. Cullen, R. Milford. Options for Achieving a 50% Cut in Industrial Carbon Emissions by 2050, *Environmental Science & Technology*. 44(6) (2010) 1888–1894.
- [3] R. Moon, A. Martini, J. Nairn, J. Simonsen, J. Youngblood. Cellulose nanomaterials review: structure, properties and nanocomposites, *Chemical Society Reviews*. 40(7) (2011) 3941.
- [4] H. Lee, S. Hamid, S. Zain. Conversion of Lignocellulosic Biomass to Nanocellulose: Structure and Chemical Process, *The Scientific World Journal*. 2014 (2014) 1-20.
- [5] D. Klemm, F. Kramer, S. Moritz, T. Lindström, M. Ankerfors, D. Gray, A. Dorris. Nanocelluloses: A New Family of Nature-Based Materials, *Angewandte Chemie International Edition* 50(24) (2011) 5438-5466.
- [6] M. Lundahl, V. Klar, L. Wang, M. Ago, O. Rojas. Spinning of Cellulose Nanofibrils into Filaments: A Review, *Industrial & Engineering Chemistry Research* 56(1) (2016) 8-19.
- [7] C. Baez, J. Considine, R. Rowlands. Influence of drying restraint on physical and mechanical properties of nanofibrillated cellulose films, *Cellulose* 21(1) (2014) 347-356.
- [8] H. Sehaqui, N. Ezekiel Mushi, S. Morimune, M. Salajkova, T. Nishino, L. Berglund. (2012). Cellulose Nanofiber Orientation in Nanopaper and Nanocomposites by Cold Drawing, *ACS Applied Materials & Interfaces* 4(2) (2012) 1043-1049.

Development of motor efficiency test setup for direct driven hydraulic actuator

Ville Koivusaari^a, Philip Westberg^b, Mikko Smolander^c, Jyrki Kajaste^d, Antti Sinkkonen^e, Panu Kiviluoma^f and Petri Kuosmanen^g

Department of Mechanical Engineering, Aalto University, Finland

^aville.koivusaari@aalto.fi, ^bphilip.westberg@aalto.fi, ^cmikko.smolander@aalto.fi,
^djyrki.kajaste@aalto.fi, ^eantti.sinkkonen@aalto.fi, ^fpanu.kiviluoma@aalto.fi,
^gpetri.kuosmanen@aalto.fi

Keywords: Electric drive, electric motor, direct driven hydraulics, hydraulics, test setup.

Abstract

Direct driven hydraulic systems have improved energy efficiency and controllability compared to traditional valve controlled hydraulic systems. Direct driven hydraulic systems control the pump's rotational speed and direction to control the flow, rather than restricting flow with valves like in traditional systems. This eliminates the throttling losses of the valves. Additionally the motor and pump can be closer to the actuator, which enables additional energy saving by minimizing friction loss of the fluid. This study presents the development of a direct driven hydraulic test setup. It is equipped with additional sensors to enable the measurement of the system's efficiency. The study includes the description of the system's components, the measurement methods and the design of the system.

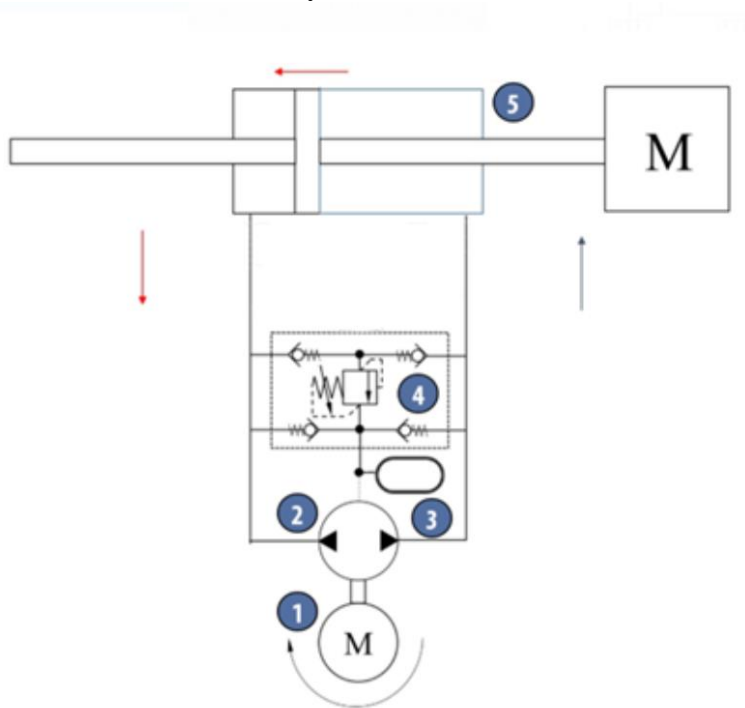
Introduction

Hydraulic systems are commonly used for industrial applications where a large force or torque needs to be produced. Today's industry is constantly trying to improve energy efficiency and reduce their impact on the environment [1]. Within different industries, there is a wide use of hydraulic systems. For example, large industry sectors where hydraulic are commonly used are construction, landscaping and forestry industries. In these sectors mobile hydraulic systems are most used way to utilize benefits of the hydraulics and typically these are valve-controlled systems.

The traditional valve-controlled systems are not very efficient due to throttled pressure losses and heat losses [2][3][4]. With new technologies and improved affordability of electric drives, direct driven hydraulic (DDH) systems have become an interesting topic for improving current valve controlled hydraulic systems. In a DDH system valves are not used for controlling the flow rate, but instead the pump's rotation is controlled to change the speed and direction of actuation. DDH systems can be more efficient and compact compared to the traditional systems, additionally they also offer improved controllability [5]. Several major companies have started to incorporate this technology on their products [6][7]. They claim that it improves the efficiency and reduces the emissions. Additional benefit of DDH is that the energy source can be brought close to the actuator to reduce energy losses, whereas in a traditional system the hydraulic fluid might have to travel a long distance between the pump and the actuator.

In this study the development of a test setup of DDH is presented. The test setup is driven by a brushless DC motor which drives a hydraulic bidirectional motor/pump. The pressure generated by the motor is then used to drive a hydraulic cylinder. The system needs to acquire all necessary data so that efficiency of different test setups can be analyzed, e.g. efficiency, power and temperature. The test setup's motor mounting needs to be modular, e.g. the motor can be easily changed to test different motors. This kind of test setup can be used for demonstrations and research purposes.

The system has two sections, one being the mechanical section consisting of the hydraulic components, the other section is the electrical consisting driving and sensing. The system is designed to move the cylinder's rod with hydraulic pump/motor which is loaded with counter weight connected to rod's end. Purpose of the system is to analyse efficiency of a different hydraulic motors, so the system needs to have modular design for the hydraulic motor mounting. The cylinder is a symmetric cylinder with a piston diameter of 63 mm and a rod diameter of 43 mm. The hydraulic power comes from a bi-directional hydraulic motor with a displacement of 1,48 cc/rev by Parker. In addition, there are also a hydraulic accumulator, hydraulic block containing pressure sensors, pressure relief valves and check valves in the system.



The electric drive is built around three major components, the electric motor, motor controller and microcontroller. The electric motor is a brushless outrunner DC motor with a power of 5300W and max voltage of 44V by Turnigy. To control this motor a programmable open source motor controller called a VESC was used. The power for the system comes from three 12V batteries in series. The logic for the system is done with an Arduino Mega. The Arduino's task is to control the actuator and also monitor the system by reading sensor and motor controller inputs to make sure that the system is working within safe margins. The main safety measurements will be temperature of the electric motor, temperature of the MOSFETS on the controller and position of cylinder's rod. Temperature is controlled with a ventilation fan and the rod's placement sensor prevents the piston from over extension during the driving cycles. For efficiency analysis, data is acquired through Arduino. To be able to measure the efficiency of the system the input and output power needs to be measured. The output power is simply the product of the torque produced by the electric motor and the revolution speed. The input power of the electric motor is the input current times the input voltage. By dividing the output with the input power, the efficiency can be calculated.

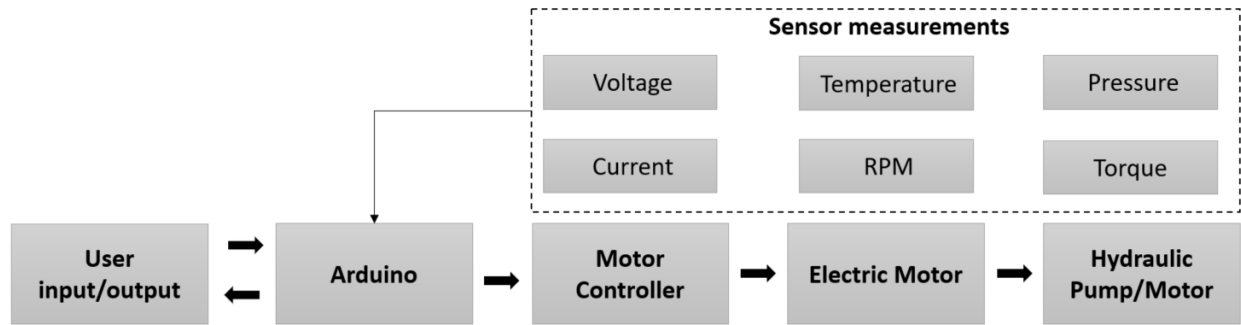


Figure 2 Electrical system

Measurement methods

The measurement is done in the Arduino, where the number of operating cycles are defined and the speed of the actuator is controlled with a potentiometer. The Arduino controls the speed by sending a pulse position modulation (PPM) signal to the VESC.

A general overview of the measurement setup is seen in fig. 2. The majority of the measurements are analog signal inputs for the Arduino. The rotational speed measurement is a digital input from a hall effect sensor. The Arduino counts the number of rotations the motor does under a certain time and calculates the RPM. For the output power measurement, the torque is measured by a force sensor which is connected to a bearing-mounted engine mount on a known distance from the center of rotation as seen in fig. 3.

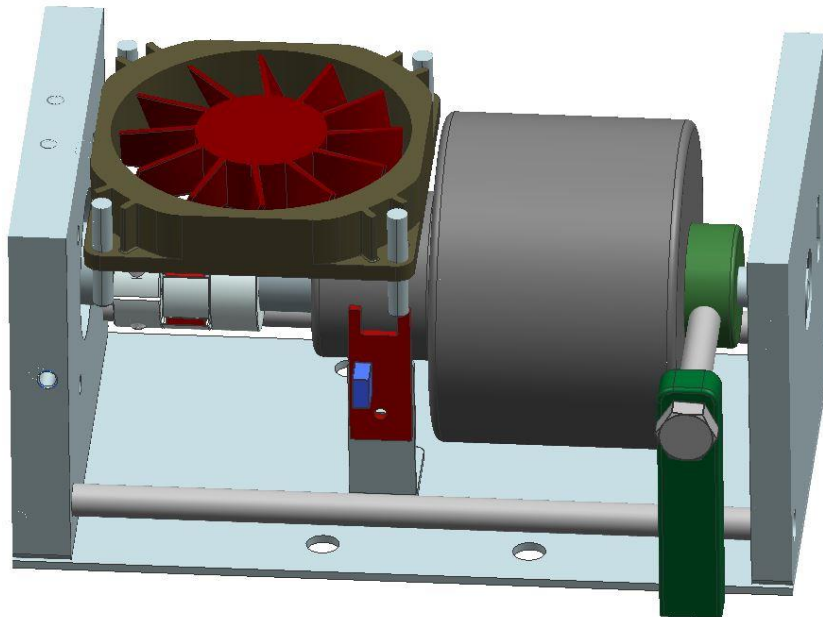


Figure 3. Model of the motor housing, where the force sensor and bearing-mounted engine mounts are indicated with green color.

For the input power the voltage and current is measured before the VESC. In this way the measurement is not the strictly measuring the efficiency of the motor, instead the combination of the motor and the controller. The voltage measurement is done with a simple voltage divider circuit so that the voltage out from the circuit is maximum 5 volts with an input voltage of 36. In that way the Arduino can measure the signal as analog input. The current measurement is done with a shunt resistor before the controller. The resistance of the shunt is small enough to not affect the motor in a considerable way. When measuring the current with a shunt resistor the goal is to measure the voltage drop over the shunt. With a low resistance this drop is so small that the Arduino can't register a difference. An instrumentation amplifier with a maximum gain of 1000 is used to amplify the signal.

Piezoresistive pressure transmitters are used to measure the pressure on both sides of the piston. These transmitters are connected to the analog input on the Arduino.

For monitoring the operation of the system, a PTC thermistor is used to measure the temperature of the motor and a magnetostrictive position sensor by GEMCO measures the rod position. The Arduino monitors these values to make sure the system is operating within its limits. In case some limits are exceeded the operation stops. The measurement sensors are either driven on 5V from the Arduino or a separate 12V power supply.

System's design

The motor housing needs to be modular so it was designed to be assembled from an aluminum block which can be changed and modified to be suitable to different motor types. The DC motor and hydraulic pump are connected with an elastomeric spider coupling. This will provide better performance when test setup is used and speed up the motor changing process. The hydraulic system is designed to be compact and all components are connected to hydraulic cylinder. This is achieved by adding a hydraulic block, which contains a pressure relief valve and all the necessary connections to hoses, pressure sensors and pressure accumulator. The system and its components are shown in fig. 4 and 5.

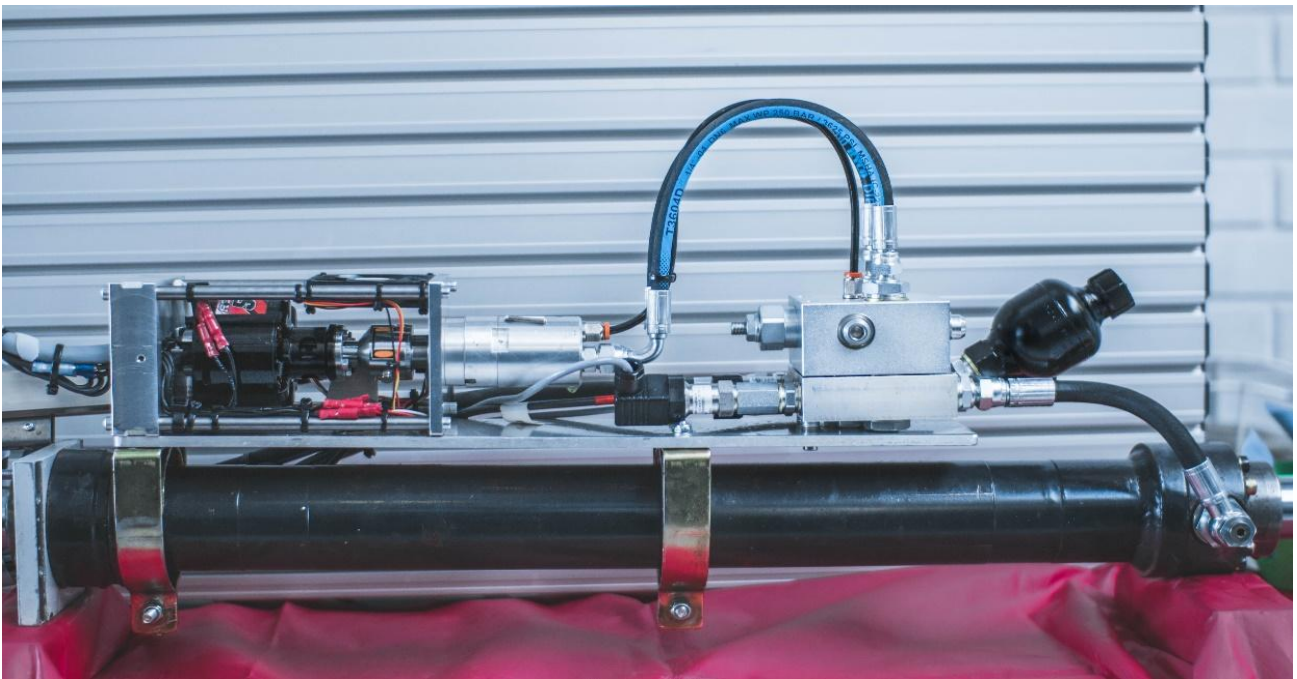


Figure 4. A side view of the system.



Figure 5. A close-up view of the motor and its housing.

Results

Our plan was to run the cylinder in cycles and measure the input and output power via Matlab. We were able to run the cylinder in cycles, but our data acquisition did not succeed as planned. Gathering data via Matlab's inbuilt Arduino tool was overwriting our code on the Arduino. This means we were unable to run the cycles and at the same time gather the information from the sensors that we had fitted. We were able to read the input power and MOSFET temperatures with the VESC-tool that came with the motor controller. The temperature of the motor was also monitored via the serial output of the Arduino to the pc.

When running the cylinder without the Matlab tool the motor was able to run the cylinder in multiple cycles effortlessly at a duty cycle of 0.35 with an input power of about 180W. The temperatures of the motor and MOSFET did not increase notably. There was no load on the cylinder when running the cycles.

Discussion

This setup has a potential to be useful, but at its current for it needs some modifications. One major improvement would be to use a designated data acquisition card. This would leave the Arduino to just run the cycles while all the data would be gathered via the designated board. The ADC resolution would also increase depending on what type of board is used, but some of the commonly used ones have an ADC resolution of 16-bit. Going from 10-bit to 16-bit is a major increase, additionally we had to use voltage dividers for most of the sensors since their output range were from 0 to 10V while the Arduino only could read a maximum of 5V, which meant that we lost additional accuracy from the measurement. This would also be avoided with a designated card that has an analog input range of 0 to 10V. Hydraulic system also need more effective bleeding system for air because time to do air removing process to this test setup wasn't desired.

There is an increased interest in design of direct driven hydraulics and this setup has a potential to help further development of these systems. That is why this project will be continued, which will hopefully lead to some interesting results.

References

- [1] Niraula, A., Zhang, S., Minav, T., & Pietola, M. (2018). Effect of zonal hydraulics on energy consumption and boom structure of a micro-excavator. *Energies*, 11(8), [2088].
<https://doi.org/10.3390/en11082088>
- [2] Minav, T., Heikkinen, J., & Pietola, M. (2017). Direct driven hydraulic drive for new powertrain topologies for nonroad mobile machinery. *Electric Power Systems Research*, 152, 390-400.
<https://doi.org/10.1016/j.epsr.2017.08.003>
- [3] Tom Sourander (2017), Sensorless position control of direct driven hydraulic actuators (master's thesis), Retrieved from:
https://aaltodoc.aalto.fi/bitstream/handle/123456789/28483/master_Sourander_Tom_2017.pdf?sequence=1
- [4] Aleksi Turunen (2018), Investigation of Direct Drive Hydraulics Implemented in Mining Loader (master's thesis), Retrieved from:
https://aaltodoc.aalto.fi/bitstream/handle/123456789/35554/master_Turunen_Aleksi_2018.pdf?sequence=1
- [5] Tatiana Minav, Carlo Bonato, Panu Sainio, Matti Pietola (2014), Direct Driven Hydraulic Drive, The 9th International Fluid Power Conference, 9, Retrieved from:
<https://pdfs.semanticscholar.org/3f29/46466de542522f001807b9552cfa2a9e0c2b.pdf>
- [6] Hitachi ZH210LC-5 capacitor electric hybrid excavator.
<https://hitachicm.com.au/products/excavators/medium-excavators/zh210lc-5>
- [7] Cat 366E H hydraulic hybrid excavator. https://www.cat.com/en_AU/articles/solutions/gci/get-the-facts-onthenewcathybridexcavator.html

Development of pressure former for continuous nanopaper manufacturing

Jami Jormakka^a, Timo Mayer^b, Tuomas Toimela^c, Panu Kiviluoma^d and Petri Kuosmanen^e

Department of Mechanical Engineering, Aalto University

^ajami.jormakka@aalto.fi, ^btimo.mayer@aalto.fi, ^ctuomas.toimela@aalto.fi, ^dpanu.kiviluoma@aalto.fi, ^epetri.kuosmanen@aalto.fi

Keywords: mechanical engineering, mechatronics

Abstract

Nanopaper is a type of paper, which consists of small cellulose fibres in the length range of nanometers, in contrast to the longer fibres of normal paper. Nanopaper generally has a lower weight, higher abundance, better biodegradability and renewability as well as higher strength and rigidity. In this study, the construction of a new machine for a new method of nanopaper forming called pressure forming will be presented. The machine was built from scratch in order to increase nanopaper manufacturing efficiency for research purposes.

Introduction

This study will cover the development of a pressure forming machine for the research of continuous production of nanopaper. Nanopaper is a type of paper, which consists of small cellulose fibres in the length range of nanometers, in contrast to the longer fibres of typical paper. Nanopaper generally has a lower weight, higher abundance, better biodegradability and renewability as well as higher strength and rigidity [1]. Significant motivation for nanopaper research has been use-cases where it can replace plastic. Nanopaper can also be used for electrical purposes by inserting highly conductive electrical circuits into the nanopaper during the manufacturing process [2].

The main challenge with nanopaper is the slowness of manufacturing. The draining and drying can require a long time, up to a few days [1]. The machine developed in this paper was constructed in order to study a faster method of producing samples for research. The pressure former unit was designed for studying the wire speed, forming pressure, paper thickness parameters and their relations when producing nanopaper with nanocellulose mass of various compositions.

Methods

Studying the pressure forming process requires the adjustment of three main parameters: wire velocity, forming pressure and thickness of the paper. The figure below, Fig. 1, shows these main parameters and their respective components. Additionally, there were some other choices which were made in order to assist in meeting the design requirements for the machine. Firstly, it was decided that there were to be four rolls (excluding support rolls) holding the belt instead of the minimum requirement of three, due to having to add a scraper on one extra roll which scraped excess scrap material off the wire. Additionally, extra space was left at the top of the frame beneath the wire for future modifications. The choices made in regards to the main components are explained in the subsequent paragraphs.

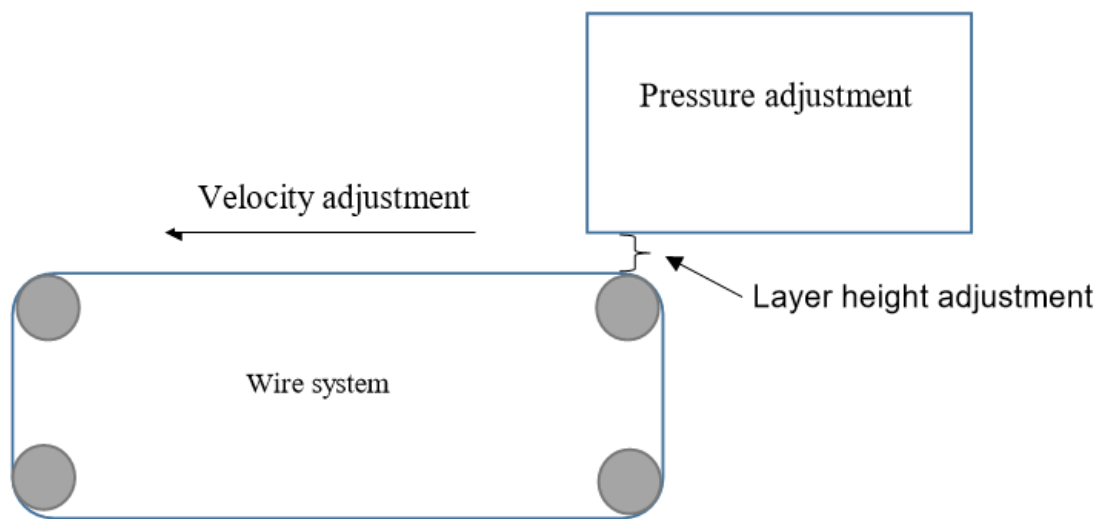


Figure 1: Main parameters and relationship between them

In the continuous pressure forming process, the nanopaper web is formed into a moving wire using air pressure of varying magnitude in order to eject a constant stream of nanocellulose out of the headbox opening. To study the effect of the wire velocity, the velocity has to be adjustable and stay constant after adjustment in order to produce uniform samples. A DC motor and transmission with high gear ratio was chosen for smooth operation. The velocity adjustment was performed microwith controller using a rotary-encoder to measure the wire belt velocity.

In order to form the nanopaper web onto the moving wire, it was necessary to deposit the nanocellulose onto the wire at a constant rate. This meant that the flow rate out of the headbox, where the nanocellulose was initially stored, had to be kept constant in order for the nanopaper sample's layer height to be constant. To achieve this, the headbox needed to be kept under a constant, controllable pressure, which needed to be matched to the wire's velocity. This was done by connecting an accurate pressure gage to the headbox which measured the pressure inside. A solenoid valve connecting the pressurised air supply to the inside of the tank was used to start/stop the air flow, and the pressure was controlled by the wall outlet in order to obtain the desired flow rate and a constant nanopaper sample thickness.

To control the layer height of the nanopaper, the headbox could be moved vertically, so that the gap between the top of the wire and the bottom of the headbox's opening was controlled to let out the right amount of nanocellulose for the desired layer height. To control the headbox's height in very small, very accurate increments (7.5 micrometers), two lead screws controlled by two stepper motors with four vertically aligned guide rails, two on either side of the headbox, were used. This was very accurate because each step was an exact angle the lead could turn and hence an exact distance that the headbox moved vertically.

Results

The pressure forming nanopaper machine was developed and tested successfully. The most important learning taken from this project was that nanopaper could be formed using air pressure. The aim had been to be able to accurately control position of headbox in increments as small as 1 μm , and this was almost successfully achieved using, and only limited to 7.5 micrometers by, the two stepper motors on the side of the headbox, as the microstepping of these could not be locked in place. The arduino code also used calibration with two switches at the top of the lead screws to make sure the headbox would be parallel to the wire with every use. As well as this, the other important

parameter of controlling the wire speed was achieved by controlling the DC motor's rotational speed which drove one of the rolls. Figure 2 below shows the finished nanopaper pressure former:

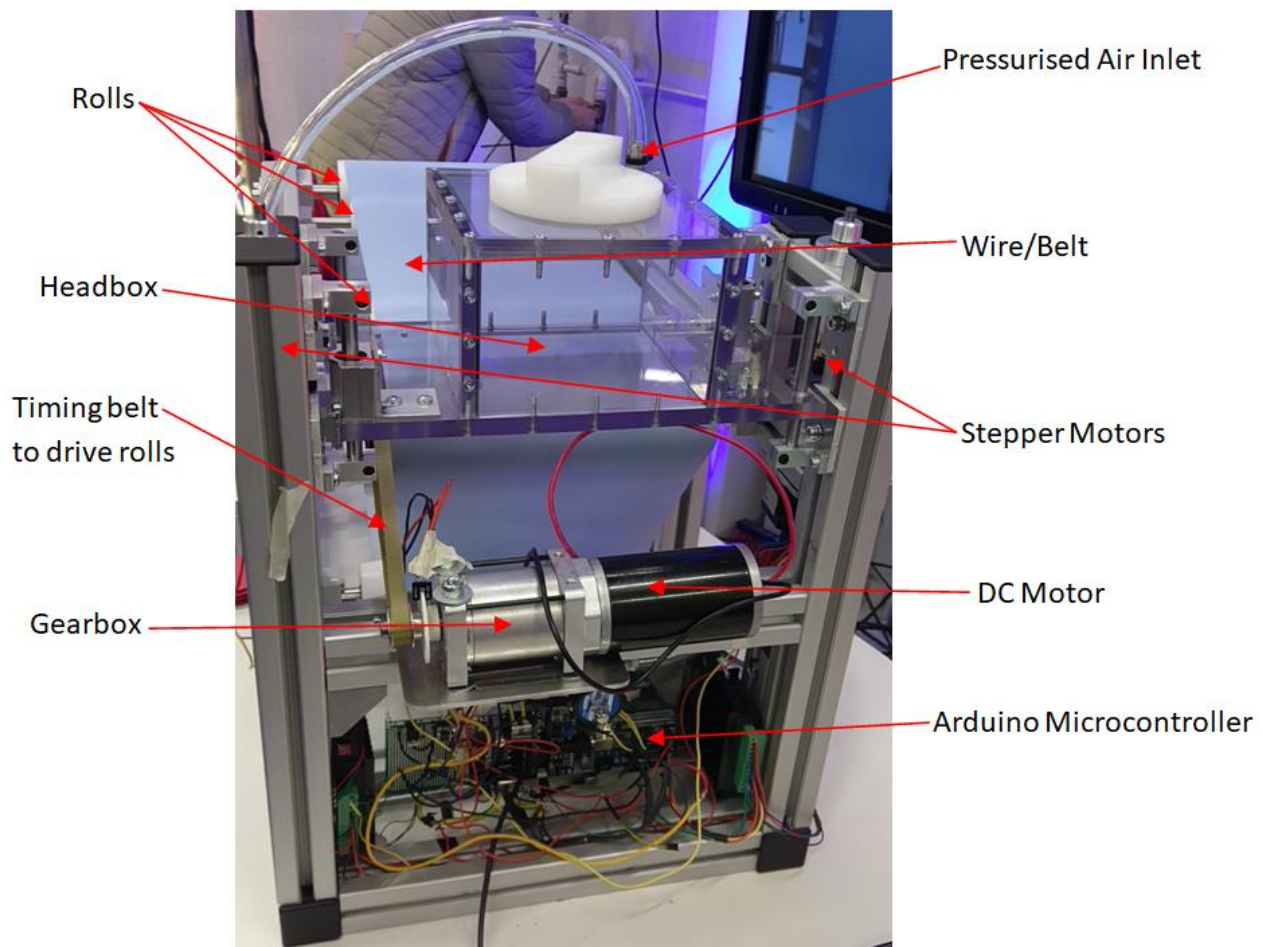


Figure 2: The finished pressure forming machine and its main components

Discussion

The most important result of this study was that nanopaper could be formed using air pressure. Pressure forming can produce nanopaper at a much faster rate than current methods as it takes only seconds for a wet sheet of paper to be on the wire whereas existing methods will take longer, with some methods taking over 120 hours for a relatively small, 201 cubic mm sample to be produced and dried [9]. Measuring the speed with an encoder wheel on the DC motor turned out to be difficult due to the significant jumping of readings from the optical switch. A positive result was that the belt tracking was eliminated with a suboptimal, makeshift wire within a few hours of running the machine and making adjustments. With a better, properly manufactured wire, the belt tracking could perhaps be eliminated even more quickly and scraping off the excess material would be made easier and smoother.

References

- [1] I. Gonzalez, M. Alcala, G. Chinga-Carrasco, F. Vilaseca, S. Bou, and P. Mutje, "From paper to nanopaper: evolution of mechanical and physical properties," *Cellulose*, vol. 21, no. 4, pp. 2599 - 2609, Aug 2014. [Online]. Available: <https://doi.org/10.1007/s10570-014-0341-0>
- [2] M.-C. Hsieh, C. Kim, M. Nogi, and K. Suganuma, "Electrically conductive lines on cellulose nanopaper for flexible electrical devices," *Nanoscale*, vol. 5, pp. 9289 - 9295, 2013. [Online]. Available: <http://dx.doi.org/10.1039/C3NR01951A>

- [3] H. Sehaqui, N. Ezekiel Mushi, S. Morimune, M. Salajkova, T. Nishino, and L. A. Berglund, "Cellulose nanofiber orientation in nanopaper and nanocomposites by cold drawing," *ACS Applied Materials & Interfaces*, vol. 4, no. 2, pp. 1043 - 1049, 2012, PMID: 22257144. [Online]. Available: <https://doi.org/10.1021/am2016766>
- [4] L. Rozenberga, M. Skute, L. Belkova, I. Sable, L. Vikele, P. Semjonovs, M. Saka, M. Ruklisha, and L. Paegle, "Characterisation of films and nanopaper obtained from cellulose synthesised by acetic acid bacteria," *Carbohydrate Polymers*, vol. 144, pp. 33 - 40, 2016. [Online]. Available: <http://www.sciencedirect.com/science/article/pii/S0144861716300819>
- [5] K. Uetani, T. Okada, and H. T. Oyama, "In-plane anisotropic thermally conductive nanopapers by drawing bacterial cellulose hydrogels," *ACS Macro Letters*, vol. 6, no. 4, pp. 345 - 349, 2017. [Online]. Available: <https://doi.org/10.1021/acsmacrolett.7b00087>
- [6] L. F. Krol, D. Beneventi, F. Alloin, and D. Chaussy, "Microfibrillated cellulose-SiO₂ composite nanopapers produced by spray deposition," *Journal of Materials Science*, vol. 50, no. 11, pp. 4095 - 4103, Jun 2015. [Online]. Available: <https://doi.org/10.1007/s10853-015-8965-5>
- [7] D. Beneventi, E. Zeno, and D. Chaussy, "Rapid nanopaper production by spray deposition of concentrated microfibrillated cellulose slurries," *Industrial Crops and Products*, vol. 72, pp. 200 - 205, 2015, special issue derived from International Conference on Bio-based Materials and Composites. [Online]. Available: <http://www.sciencedirect.com/science/article/pii/S0926669014007109>
- [8] S. Lingaiah and K. Shivakumar, "Electrospun high temperature polyimide nanopaper," *European Polymer Journal*, vol. 49, no. 8, pp. 2101 - 2108, 2013. [Online]. Available: <http://www.sciencedirect.com/science/article/pii/S001430571300222X>
- [9] H. Sehaqui, A. Liu, Q. Zhou, and L. A. Berglund, "Fast preparation procedure for large, flat cellulose and cellulose/inorganic nanopaper structures," *Biomacromolecules*, vol. 11, no. 9, pp. 2195 - 2198, 2010, PMID: 20698565. [Online]. Available: <https://doi.org/10.1021/bm100490s>
- [10] S. Lingaiah, K. Shivakumar, and R. Sadler, "Electrospun nanopaper and its applications to microsystems," *International Journal for Computational Methods in Engineering Science and Mechanics*, vol. 15, no. 1, pp. 2 - 8, 2014. [Online]. Available: <https://doi.org/10.1080/15502287.2013.833996>

Device for tree volume measurements

Teemu Laine^a, Simo Lindholm^b, Viljami Pirttimaa^c, Panu Kiviluoma^d and Petri Kuosmanen^e

Department of Mechanical Engineering, Aalto University, Finland

^ateemu.laine@aalto.fi, ^bsimo.lindholm@aalto.fi, ^cjuuso.pirttimaa@aalto.fi, ^dpanu.kiviluoma@aalto.fi, ^epetri.kuosmanen@aalto.fi,

Keywords: Biomass, Carbon storage, Biofuel, Forest, Buoyant force

Abstract

Approximating the complete biomass of a forest will be essential for the biofuel and carbon storage industries in the future. Current methods are optimized for measuring the trunk volume of the trees which is sufficient for the traditional wood industry but as much as half of the biomass is contained in the branches. This paper presents a device that provides accurate measurements the tree volume and density including branches. The device can be used for improving the existing mathematical models to get a more accurate estimate of the total biomass in the forests. Measurement accuracy of the presented device was evaluated by measuring a reference object of known volume, which proved that the device produces accurate data.

Introduction

Finland has the highest proportion of total energy production with biomass compared to any other industrialized country. Most of the biomass used for energy production is wood (2017) [1] and the usage of biomass for energy production has increased over the years. Therefore, it is important to be able to measure how much biomass is stored in the forests. Another interesting future prospect is carbon storage in forests. In order to estimate the carbon storage capacity of the forest, accurate estimate of the biomass needs to be known. [2]

Volume estimation is currently done by using mathematical models. These mathematical models do not take branches into account, even though their volume is significant. [2] Accurate estimation of the volume is also necessary to determine the density of a tree. Many structural properties of the tree depend on its density. For example, tensile strength of a pine tree fell in spring is only 1/6 of pine fell in the summer due to the difference in water content and density. [3] This means that the applicability of a tree is determined by its density.

A traditional but still widely used method for estimating trunk volume is using a Biltmore stick. The Biltmore stick is a calibrated instrument that is held at an arm's length away from the eyes of the user. The stick has a scale that indicates the breast height diameter of the measured tree. [4] This method is quick, easy and non-destructive. However, it is only used as a rough estimate of the usable trunk volume, but it is a poor estimate of the biomass of the whole tree.

A more modern method for volume measurement is using terrestrial laser scanning (TLS). This method allows tree volume measurement without cutting the tree into pieces. With this method, the tree is first digitized by TLS. Then the TLS data is processed by geometric fitting algorithms which can compute the total volume of the measured tree. This method does not take into account branches that are smaller than 7 cm in diameter, which leads to ± 30 % error in branch volume measurement. This error is significant, and the results do not include the density of the tree. [5]

University of Helsinki has a volume measuring device in Hyytiälä forestry field station, which has been developed in collaboration with Aalto University. The device measures volume of a tree piece by immersing it in water. Force sensor registers the buoyancy and determines the volume with

Archimedes' principle. However, based on feedback given by the users, the existing measurement device isn't reliable enough. It has a suboptimal load cell and it is tedious to use since it needs to be operated manually. The measured object has to be loaded with a ladder at a great height which is inconvenient. The lowering mechanism is based on a winch which generates severe fluctuations to the measured buoyant force. While the current device is still currently being used, the need for an improved device is apparent. The goal of this paper is to present a new version of the measurement device which was developed at Aalto University.

Device for Volume measurement

The mechanical concept of the volumeter is illustrated in figure 1.



Fig. 1 Structure of the device consists of a tank (1), a specimen holder (2), a stepper motor (3), a counter weight (4), a linear actuator (5), a load cell (6), a ultrasonic sensor (7) and a valve (8).

Volume measurement is started by filling the water tank (1) and powering up the system. Operator of the machine attaches the specimen to a holder (2). The holder is on the ground in the beginning of the measurement. Measurement cycle is started by the operator. The machine starts to lift the holder by rotating a stepper motor (3), which is connected to a timing pulley. Counter weight (4) makes sure that the timing belt does not slip from the gear wheel. When the holder is lifted up, the machine starts to move the holder in horizontal direction. This is done with linear actuator (5). Stepper motor (3) rotates at the same time so that the holder does not move vertically. When the holder is on top of the water tank, it is lowered with the stepper motor. Force that is acting on the timing belt is measured with a load cell (6). Volume of the measured part can be calculated from the buoyancy effect (change in force readings). Calculations take into account that the immersion depth depends on the rising water level in the tank. Water level is measured with ultrasonic sensor (7), which is placed inside a

tube to mitigate waves. Measurement cycle ends when the machine has moved the holder back on the ground, next to the water tank. After the measurement, operator can drain the water tank with a valve (8).

Table 1 Selected components

Component	Selected part	Reason
Tank	270-liter air tank, 50 x 149 cm	Tall and narrow, mounting feet, price vs. custom-made stainless-steel tank.
Lifting mechanism	Belt drive with stepper motors.	Economic way of producing long lifting movement. Open-loop control is sufficient, so the lowering height does not have to be measured.
Water level measurement	Ultrasonic sensor MB7369	Does not need a float to sense the water surface.
Load cell and amplifier	KD24s 50 kg S-type load cell and Sparkfun HX711 amplifier	Load cell is suitable for measuring tension. Amplifier is inexpensive and it has 24-bit resolution and 80 Hz sample rate.
Temperature measurement	DS18B20 digital thermometer	Easy to use 1-Wire interface, $\pm 0.5^{\circ}\text{C}$, Accuracy
Software	Python-based Jupyter Notebook	No licensing costs, easy development
Computer hardware	Arduino Nano and Raspberry Pi 3B+	Arduino can run the motion control and read the sensors in real time. Raspberry Pi makes networking easy and is suitable for data processing.

The accuracy and repeatability of the volumeter was tested with a reference object whose dimensions and weight are known. Comparing the measured volume against a calculated value at different submersion heights showed the measurement error of the system. This is illustrated in figure 2. Comparing the results between multiple measurements makes it possible to evaluate the repeatability of the measurement system.

The reference object is an 80 x 219 mm steel cylinder whose volume is 1100 ml and weight 8.62 kg. Water temperature was 8°C during the measurements which means its density was 1000 kg/m^3 .

First the empty specimen holder was measured to record its volume at different immersion depths. Then the reference object was attached to the specimen holder and a new measurement cycle was made. The volume of the reference object was calculated by subtracting the measured volume of the specimen holder from the second measurement. Moving average filtering was used on the force measurement data to filter noise. Due to time constraints, the reference object was measured only three times, which leaves the repeatability of the system uncertain. The results of the measurements are compared against a theoretical value in figure 3.

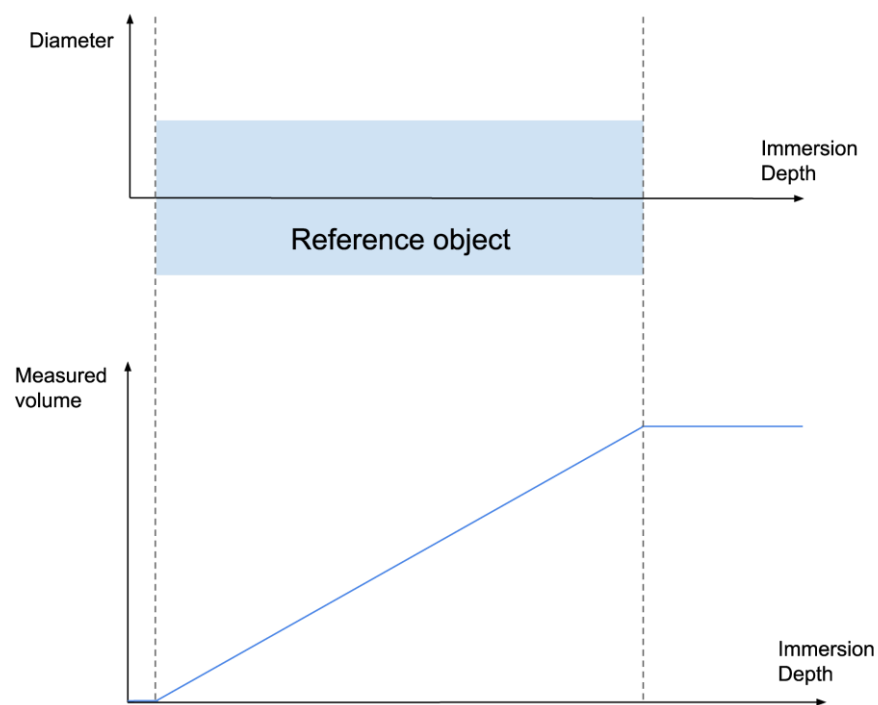


Fig. 2 Illustration of the used test method

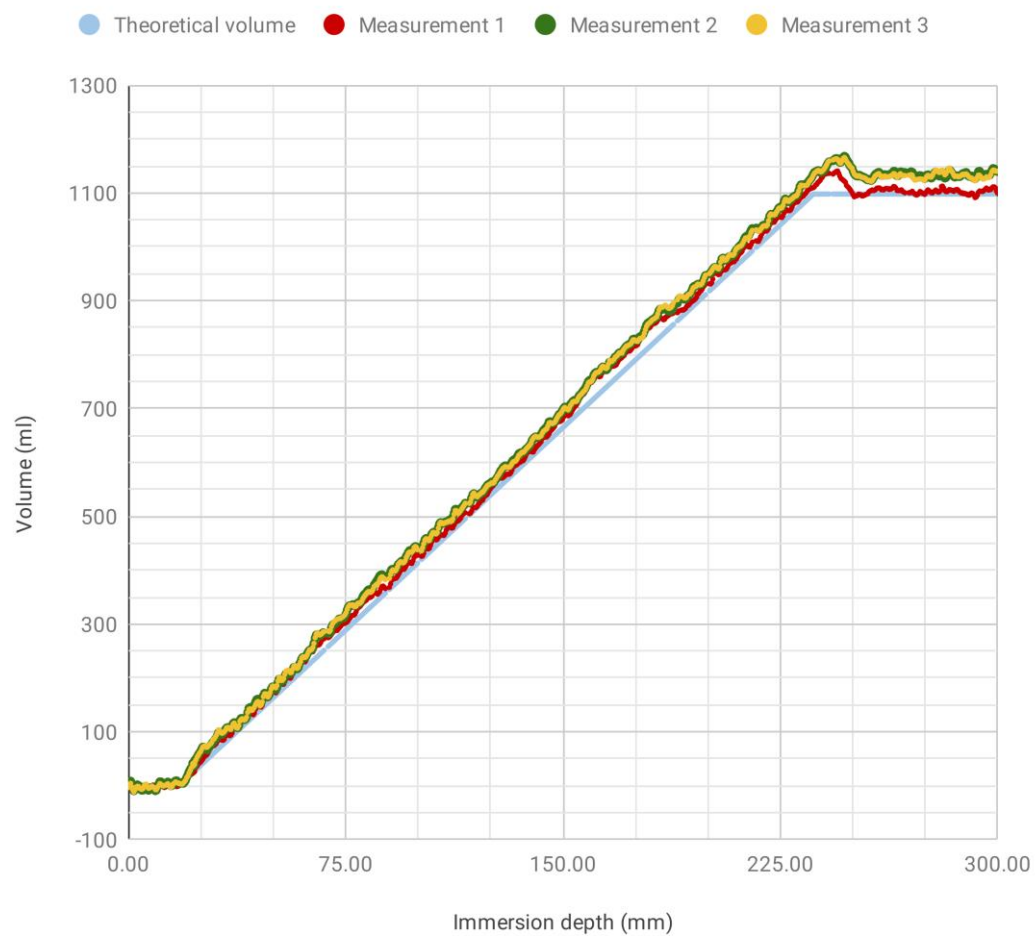


Fig. 3 Measurement data

Conclusion

The main goals of this study were achieved as the new volumeter has improvements to correct the shortcomings of the previous device. Usability has been greatly improved as the specimen can be loaded on the ground level without a ladder. The automated test cycle makes it possible to keep the user interface as simple as possible. The greatly improved drive system produces smooth and reproducible movement regardless of the load. Water level rise is measured and compensated in the measurements with the ultrasonic surface level sensor. Temperature measurement is used for compensating small differences in the density of the water.

Another goal for the new volumeter was to produce as accurate data as possible. Figure 3 shows that results of the measurements are close to theoretical values. Only at the end of the immersion, the values deviate significantly from the theoretical value. Measured volume continues to climb after the submersion depth reaches the length of the reference object. This is probably due to the surface tension of the water (Fig. 4). Error in the measured volume decreases when the reference object is lowered deeper into the water tank and the air pocket on top of the object collapses.

Total measured volume is calculated by averaging measurement values of the fully submerged object. Error in the total volume of the reference part was +0.18 % in the first measurement, +3.04 % in the second measurement and +2.88 % in the third measurement. Increased error in the second and third measurement was probably due to the water that was on the surface of reference object and the holder from the previous measurements. The object and the holder are weighed before every measurement and the buoyant force is calculated by comparing the initial weight to the measurement data. Weight of the water on the object before the submersion is therefore calculated as buoyant force.

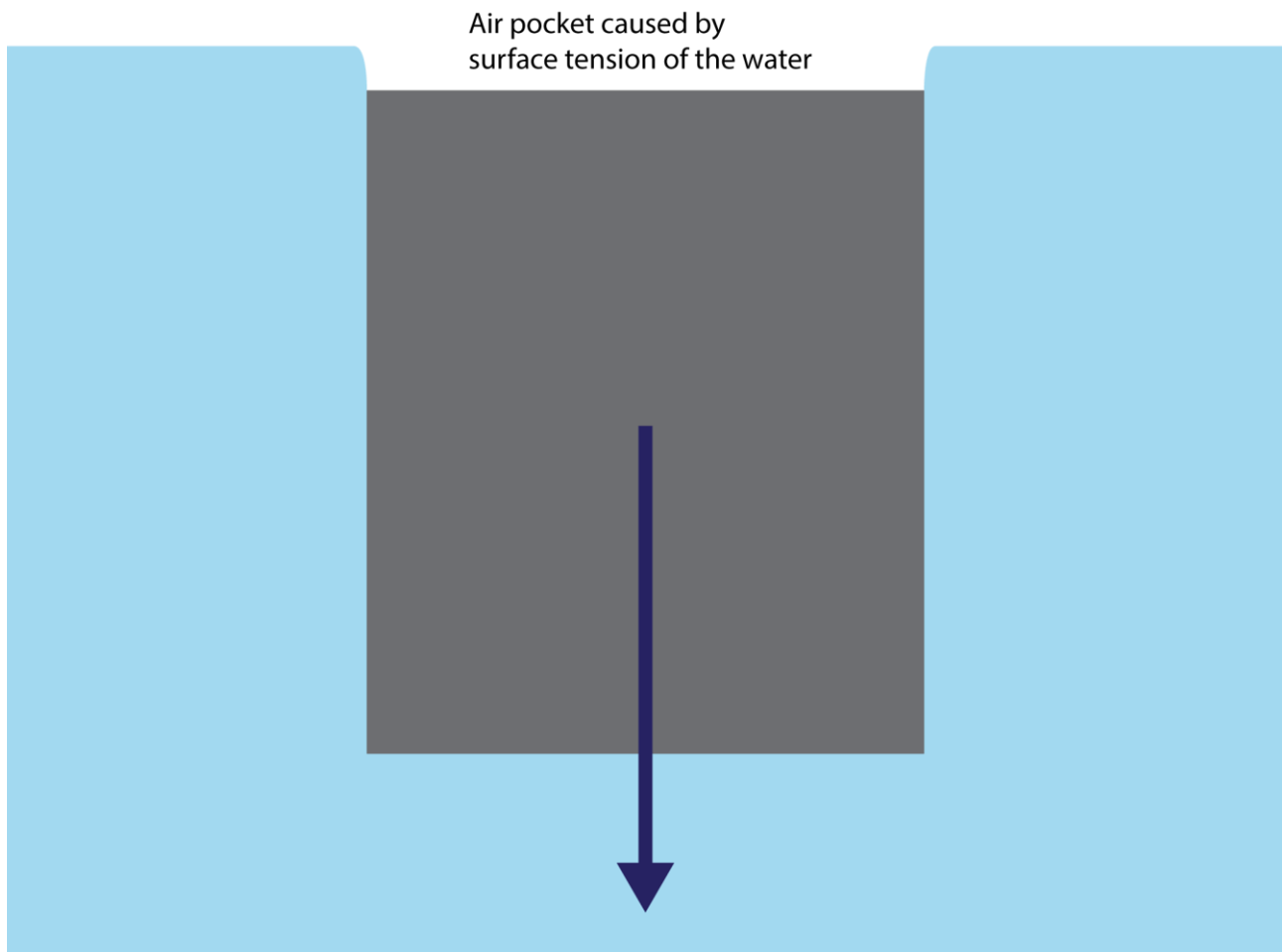


Fig. 4 Visualization of surface tension of water

The test results demonstrate that the device presented in this paper is suitable for volume measurements. The method used, enables continuous volume measurements throughout the length of the specimen. The device produces results that are competitive in accuracy with other volume measurement methods.

Measurement with terrestrial laser scanning or Biltmore stick are not as reliable and they do not give the density of the specimen. Furthermore, Biltmore stick can only estimate the trunk volume of the tree which is insufficient for estimating the total biomass of a forest. Accuracy of TLS in terms of branch volume is $\pm 30\%$, which is ten times worse than the accuracy achieved in this study [5].

5 % of detergent in the water has been used to reduce surface tension in similar measurements [6]. Using warmer water will reduce the surface tension even more. These improvements can be studied in further studies to see if they improve the accuracy of the measurements.

Reinforcing and stiffening of the frame of the device could reduce fluctuations in the load cell readings. It would also allow faster movement of the specimen, which would reduce the cycle time of the measurements. Stiffer frame could be achieved with thicker rectangular hollow section beams and gussets. Another option would be to add angled supports to the vertical beams. Vertical beams of the frame were built by connecting two separate beams end-to-end for easier shipping of the device. However, this unnecessary joint reduces stiffness.

Production version of the measurement and control software for the volumeter is still under development. The final version will automate the calibration, measurement cycle, data capture and data processing. When these features are implemented it is feasible to do more thorough repeatability and reproducibility studies with the volumeter.

References

- [1] “Wood based energy,” Maa- ja metsätalousministeriö. [Online]. Available: <https://mmm.fi/en/en/forests/use-of-wood/wood-based-energy>. [Accessed: 10-Mar-2019].
- [2] R. P. Yadav, B. Gupta, P. L. Bhutia, J. K. Bisht, and A. Pattanayak, “Biomass and carbon budgeting of land use types along elevation gradient in Central Himalayas,” *J. Clean. Prod.*, vol. 211, pp. 1284–1298, Feb. 2019.
- [3] “Strength properties of wood,” Wood Products, 13-Nov-2013. [Online]. Available: <https://www.woodproducts.fi/content/wood-a-material-1>. [Accessed: 10-Mar-2019].
- [4] E. R. Wilson, J. Murray, I. Rydning, and E. Casson-du Mont, “Comparison of three tools for measuring tree diameter in stands of different age and tree size,” *Q. J. For.*, vol. 101, pp. 267–274, 2007.
- [5] M. Dassot, A. Colin, P. Santenoise, M. Fournier, and T. Constant, “Terrestrial laser scanning for measuring the solid wood volume, including branches, of adult standing trees in the forest environment,” *Comput. Electron. Agric.*, vol. 89, pp. 86–93, Nov. 2012.
- [6] J. M. Chen, P. M. Rich, S. T. Gower, J. M. Norman, and S. Plummer, “Leaf area index of boreal forests: Theory, techniques, and measurements,” *J. Geophys. Res. Atmospheres*, vol. 102, no. 24, pp. 29429–29443, 1997.

Effect of external load on rotor vibration

Mikko Barinoff^a, Heikki Lagus^d, Joonas Stenman^c, Risto Viitala^d, Panu Kiviluoma^e and Petri Kuosmanen^f

Department of Mechanical Engineering, Aalto University, Finland

^amikko.barinoff@aalto.fi, ^bheikki.lagus@aalto.fi, ^cjoona.stenman@aalto.fi, ^dristo.viitala@aalto.fi
^epanu.kiviluoma@aalto.fi, ^fpetri.kuosmanen@aalto.fi,

Keywords: Paper machine roll, external load, rotor dynamics, vibrations, damped system, viscous damper

Abstract

Rotor dynamic has a major impact to the end product in paper production and thus it is widely been researched for decades. In general, the behavior of rotors is studied only without an external load and research with the load is scarce. However, an unloaded arrangement does not correspond to a real situation. The aim in this study is to develop an external loading device for a rotor and investigate the effects of the external load on a rotor. It is supported by Academy of Finland (TwinRotor, grant number 313675). Since the point of our interest are the loading conditions in a paper machine and the test rotor is paper machine roll, the amount of the load are taken from real paper production conditions as well. There paper machine rolls are under 10 kN/m distributed force exerted from a paper web. In this study, the load is conducted with a relatively narrow belt to the rotor. Thus, developed force can be concerned to be a point load. To achieve similar forces as in the real situations the loading force should be 40 kN, since the test rotor body is 4.0 m long. However, the used force is lower, because a same deflection is achieved with lower force using the point load comparing to a distributed load. The effect of the load on the rotor vibrations is investigated with laser run-out measurements. Measurements are taken with two different loads, in which rotational frequencies from 4 Hz to 18 Hz are used with an increment of 2 Hz. After a signal analysis the frequency response of the rotor with these two loads can be examined; some force amplitudes increased considerably at a specific frequency under the larger load. The observations are presumably results of the bending stiffness variation of the rotor. The study proves the developed system functioning and suitable for simulating external loads of a rotor.

Introduction

Paper industry is still a remarkable field in Finland, as the total production in 2016 was over ten million tons, from which 9.6 million tons went to export. Paper consumption globally has steadily increased, and in 2017 the consumption was 407 million tons. [1]

The behavior of a paper machine roll under static loads caused by the paper web has significant impact to the paper quality as well as the efficiency and reliability of the process. Especially the vibration of the paper machine roll causes many troubles in the paper manufacturing process, and the constantly increasing quality requirements of paper lead to the higher quality requirements of critical rotor components as well. In this context, the bearings of the paper machine roll are the most critical component, since they sustain the excited vibration. The vibration of the paper machine roll influences e.g. to the thickness, surface quality and structure of the paper been processed. In addition, for the sake of cost-effect structure and manufacturability of the rotor, understanding this behavior is important. [2]

Previous study is done without the external load. The external load is a significant factor in real-world solutions and thus, the repetition of the past experiments related to a rotor vibration with an external load is relevant. For example Viitala has showed in his doctoral dissertation that bearing geometry errors excite subcritical rotor vibration. The shape of the bearing inner ring determines the frequency of the excitation; an oval shape excites vibration two times per revolution and a triangular shape three times per revolution. However, although the bearing inner ring would be perfectly circular, it can be deformed by noncircular shaft end or clamping. In this situation the bearing inner ring adapts the part of the shape, where it is being mounted. Viitala has showed that these excitations can be reduced by forming the inner ring and achieve great results. These measurements have been made with same test rotor environment as in this research but without an external load. [3]

The aim in this study was to examine the effect of an external load on rotor vibration. The external load was generated with a point loading device, which was built for this purpose. The external load was selected to be similar to the production conditions in the paper industry. This present study investigates also the feasibility of the point loading device. The point load was computationally validated to correspond to a distributed load in production environment; theoretically the point load of the device cause the same deflection to the rotor as the distributed load of a paper web.

Methods

The test setup consisted of a rotor (paper machine roll), supported by two SKF 23124 roller bearings. The custom-made split bearing housings were mounted on rigid steel jacks, which were fastened to guiding rails on the concrete foundation in test environment. An electric motor was connected to the rotor with universal joint.

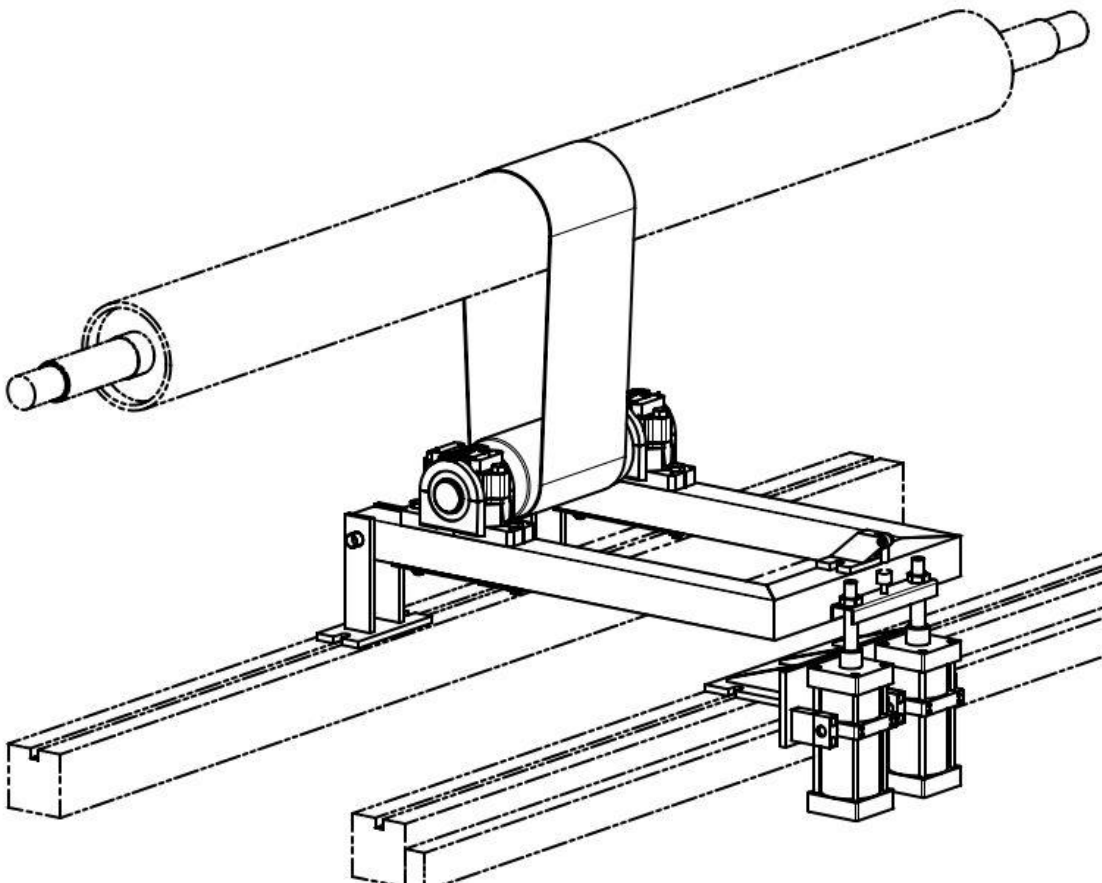


Figure 1 Loading device consisting of loading roll, belt, frame and pneumatic actuators

The loading device was included to an existing testing setup to simulate different loading conditions. This testing setup and loading device are demonstrated in Figure 1. The paper machine roll was loaded with the 400 mm wide Siegling Extremultus GT 40P tensioned belt, which generated a downward force to the rotor. The loading roll with two SKF 1222 K -bearing units was fastened to the lever mechanism. The lever frame was hinged at one end, and the other end was jointed to two SMC C92SDB 160-250 pneumatic cylinders which could theoretically generate 110 kN force against the rotor. The force sensor was placed between the cylinders and the lever frame enabling a dynamic force control during the operation. The load was measured and controlled through a commercial LabView software. The belt tension force was calculated by multiplying the measured load value with the lever coefficient, which the frame geometry was determined. The cylinder pressure was controlled with the SMC electronic pressure controller, which was connected to LabView's PI-controller. In addition the pneumatic system was equipped with the mechanical pressure control valve to prevent belt damage. The control system schematic and the selected components are presented in Figure 2.

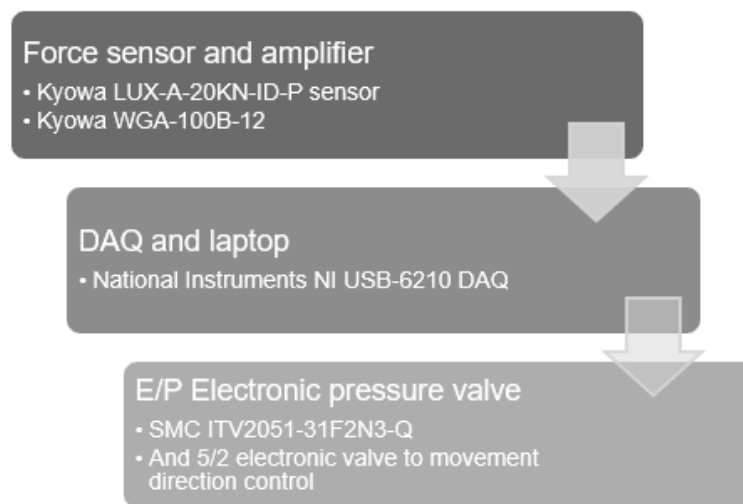


Figure 2 Control diagram of the loading system

In production conditions, the paper web tension can be as high as 10 kN/m [2]. This gave a 40 kN uniformly distributed load against used four meters long paper machine roll. The analysis of beams showed, that if a uniformly distributed load q_0 over a beam (length L) was replaced with a $5/8 * q_0 * L$ point load at the middle of the beam the maximum deflection was equal. According to belt manufacturer specs, a 400 mm flat belt was chosen to be used to transmit the load on the paper machine roll. The rotor diameter and allowed belt bending radius limits the thickness of a belt. To achieve required strength to withstand belt tension, it is necessary to select at least 400 mm wide belt. FEM analysis showed, that 25.5 kN load with 400 mm wide belt provides approximately equal maximum deflection as a 40 kN distributed load or a 25 kN point load. The deflection of the rotor with the distributed load, the point load and their difference as the function of the axial position are shown in μm in Figure 3.

The run-out of the rotor was measured with a laser sensor Matsushita NAIS LM 300 displacement sensor fixed on the arc frame around the rotor. Total of 16 data sets were measured, since the measurements were taken at rotating frequency range from 4 Hz to 18 Hz with increments of 2 Hz and this procedure were repeated with loads of 12.5 kN and 25 kN. At each rotating frequency 100 revolutions were measured. Measurements were triggered with a rotary encoder Heidenhain ROD 420, which had resolution of 1024 (pulses/rev.). This triggering method ensured that measurement samples were acquired at the same phase in every revolution of the rotor. The test setup is presented in Figure 4.

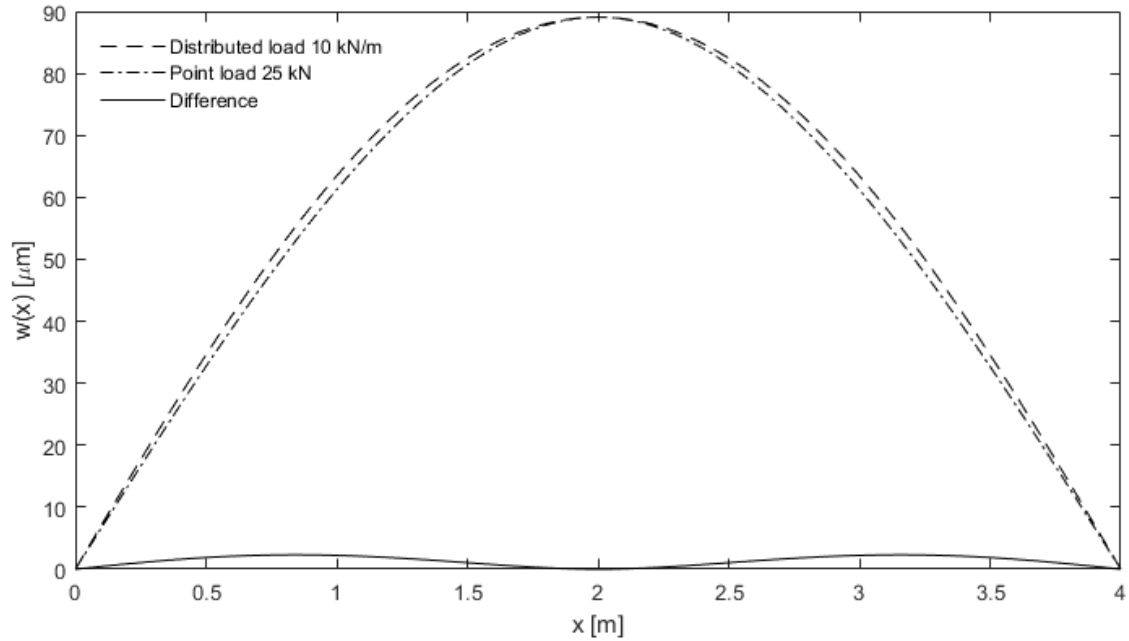


Figure 3 Deflection of roll comparing point load and distributed load

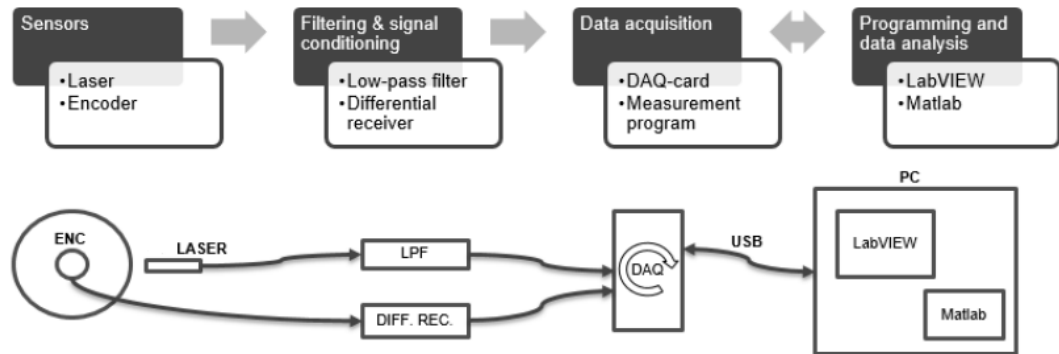


Figure 4 Measurement system [3]

Results

Measurements were done with two different loads (12.5 kN and 25.0 kN) and with eight different rotational frequencies between 4 Hz and 18 Hz. Results are shown in Figures 5 and 6. All measurement data was processed with Fast Fourier Transform (FFT), which presents the data in the frequency domain. The harmonic components are force periods per one revolution. Because the sampling was triggered by the encoder using 1024 sample per revolution instead of the time, results are shown by harmonic components. The first harmonic component is removed from the figures because it is an error from roll surface and centerline deflection. Also any significant influence cannot be distinguished from it related to the varied load. The higher harmonic components are the results of the excitations, which occur multiple times per revolution.

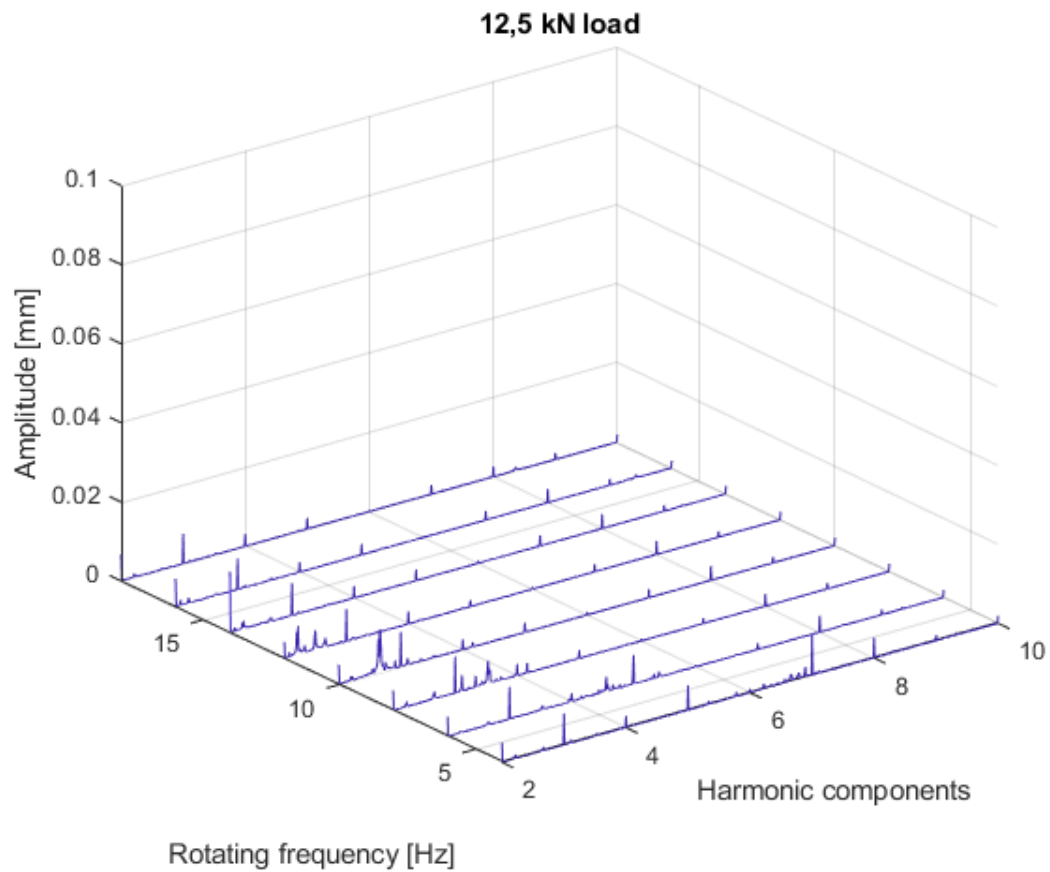


Figure 5 Vibration measurements at rotation frequencies between 4-18 Hz and 12.5 kN load

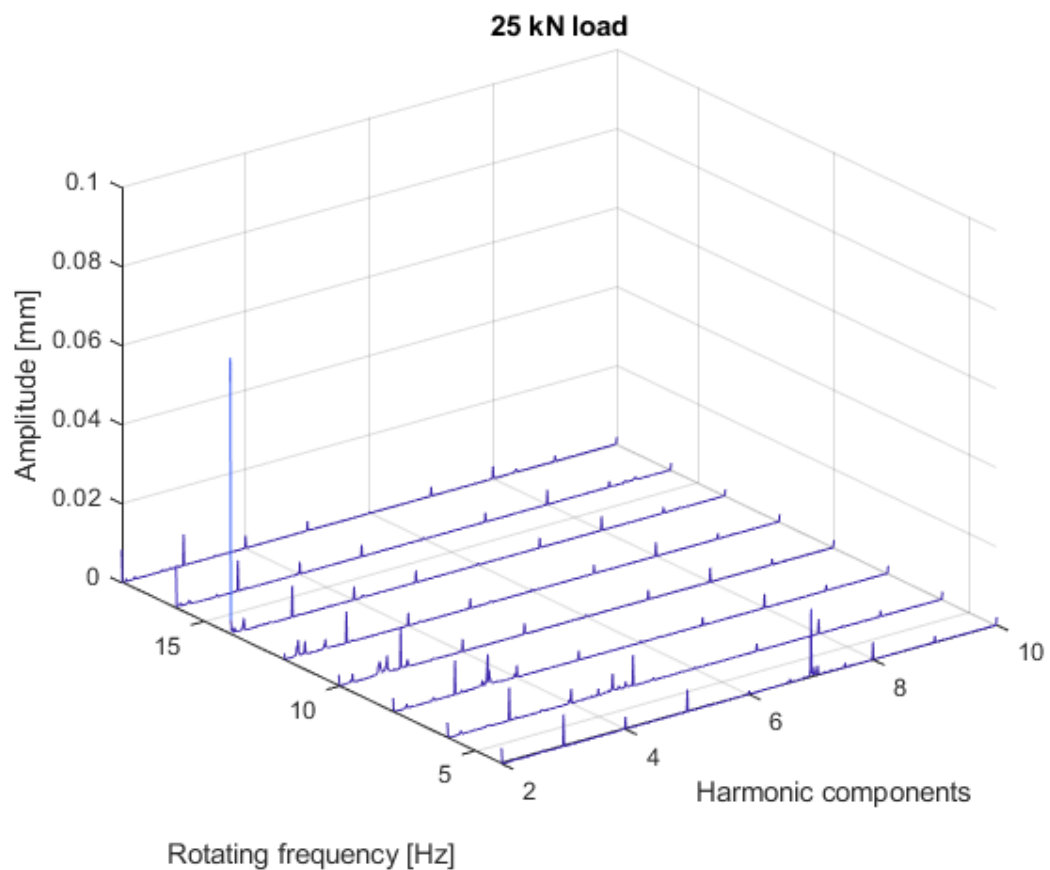


Figure 6 Vibration measurements at rotation frequencies between 4-18 Hz and 25.0 kN load

Discussion

Interpreted from Figures 5 and 6, the vibrations on the second harmonic component are seemingly larger on 14 Hz with the 25 kN load. This may be the effect of the bending stiffness variation of the test rotor. The effect increases according to deflection of the rotor. On the other hand, the tension belt has damping effect, which reduces the amplitude. Anyway, in this test setup it is not possible to separate damping effect from the results. Also, because the rotating frequency increments were relatively large, the results could miss some subcritical resonances in between these increments.

The 1-point vertical position measurement was used in this research. This method does not exclude the error coming from the eccentricity of the rotor, but can be eliminated in the further research by using the same 4-point method measurement as in Viitala's research [3]. Anyway, the measurement method used in this case was good enough to indicate the effects of the external load on the rotor deflection.

The loading device designed and constructed for this research project proved to work and perform as expected for the most part. The belt structure turned out to be problematic, because the seaming of the belt caused some vibrations, which were notable on the rotor. In addition, when the system was running without load, the loosened belt caused significant vibrations to the rotor. The results showed good repeatability, which indicates that the developed loading system is suitable for simulating external loads of a rotor.

Acknowledgements

This work was a part of Digital Twin of Rotor System –project (TwinRotor, grant number 313675) that was supported by Academy of Finland.

References

- [1] Finnish Forest Industry Federation, 6.3.2019, available:
<https://www.forestindustries.fi/statistics/pulp-and-paper-industry/>
- [2] University of Oulu, Dept. of Mechanical Engineering, Machine Design Laboratory, 464074S
Paperiteollisuuden koneet osa 2
- [3] Viitala, Raine. 2018. Effect of Assembled Bearing Inner Ring Geometry on Subcritical Rotor Vibration.

Granular jamming based gripper for heavy objects

Patrick Frilund^a, Iiro Vuorinen^b, Jesse Miettinen^c, Panu Kiviluoma^d and Petri Kuosmanen^e

Department of Mechanical Engineering, Aalto University, Finland

^apatrick.frilund@aalto.fi, ^biiro.vuorinen@aalto.fi, ^cjesse.miettinen@aalto.fi,

^dpanu.kiviluoma@aalto.fi, ^epetri.kuosmanen@aalto.fi

Keywords: Granular Jamming, Crane, Lifting, Universal Gripping

Abstract

Moving of heavy objects with overhead cranes requires the operator to fasten the object to the hook via ropes or chains. This is a time consuming process, which would be avoided with universal grippers, that can lift objects regardless of shape. In this paper the scalability of granular jamming grippers for crane applications by designing and building a large scale grippers using simple materials and different granular materials has been studied. Objects of different shapes and sizes were successfully lifted with certain gripper configurations. The results showed that grain size and grain compressibility both affect the performance of the gripper. It was shown that in order to efficiently lift heavy objects with granular jamming the granular material has to not only be able to compress sufficiently in the vacuum but also have large enough stiffness. With this setup, gripper based on the granular jamming was able to lift objects with various shapes and weights up to 120 kg.

Introduction

The technology around lifting heavy objects has always relied on strong hooks and some manual labour for attaching the target object in various ways to the hook. Conventionally in overhead crane lifting, the objects to be lifted are attached to the hook via chains or ropes. This system, having two mass nodes attached via ropes is both, slow and prone to double pendulum dynamics [1]. Also, this system requires workers to constantly work around the dangerous environment around the hook.

In order to achieve more efficient and safer crane lifting, a universal gripper could be implemented. Universal gripper could save a lot of time for crane operators. Currently crane operators have to use a lot of time for attaching their target object somehow to another object that can be lifted with a hook. Thus a lot of time could be saved with a universal gripper. Universal grippers are such that can lift objects with variable shapes [2].

Gripping technology in robotics has taken lots of big steps recently towards universal gripping. Shortly put, gripping technologies can be divided naturally in to 3 different categories; actuation, controlled stiffness and adhesion. Actuation basically covers all of the traditional gripping technologies, such as different rigid jaw grippers and stiff grippers driven by complex algorithms. It also covers the compliant materials that deform during the gripping process and thus dividing the pressure evenly [3]. The problem with actuation based grippers is that they can be rather clumsy with various shapes and can even cause harm with applied normal forces [4].

Adhesion based grippers are able grip objects with a shear force that is applied to lifted object. This kind of lifting method can be used to lift large, deformable and easily breakable objects. One way of making an effective adhesive gripper is to put very thin and adhesive micro-sized planes or hairs on the gripping surface. When the gripping surface has been placed on the object and applied with shear-force, the contact area between the object and the bending micro planes grow. A simple way to intuitively understand this phenomenon is to simply imagine a gecko walking a straight wall. This technique can be used to lift without squeezing objects even in the range of few kilograms [4].

The idea behind controlled stiffness is that the gripper can be deformed in its soft configuration to surround the target object [3]. After the gripper has surrounded the target object, the gripper is then stiffened and thus it forms a grip around the target object. One example of this is granular jamming where there is a tight and air-sealed pouch filled with granular material. When the pouch is at its soft configuration, it can deform easily as its contents can be considered as fluidic in macro-scale. After the air between the granular mass has been sucked out, the granular contents get jammed and the pouch stiffens to its deformed shape around the target object [5]. The granular jamming process can even be quickened by adding positive pressure during deformation and releasing stages in the gripping process [6]. Stiffness can be controlled also in alloys that change their phase in depending on the temperature. There are also some fluids that respond to electric and magnetic fields by changing their viscosity [3].

Development in the robotics industry has led to promising results in lifting with granular jamming [3]. For example, Empire Robotics has successfully lifted objects with a mass of around 10 kg with a 16.5-cm-diameter-gripper [7]. Thus, the technology might be viable option for substituting some of the crane lifting done with ropes and objects weighing under few hundreds of kilograms. However, it is still unconfirmed what the maximum capacity of this lifting methods is. This paper documents the scalability of granular jamming based gripper by scaling the size of the pouch and trying different granular materials as the medium.

Calculations for lifting of cylindrical shapes

The lifting capabilities of a granular jamming based gripper are hard to calculate exactly, since they are conditional on the shape of the object. The gripper consists of a large pouch filled with granular material, a body to support the pouch and a vacuum pump. The gripper assembly is lifted on top of a cylindrical object, with radius r and height d (fig. 1a). Below, the maximum lifting capacity for lifting of a cylindrical shape is approximated analytically. In order to simplify the calculations, this approximation is done for a cylindrical shape.

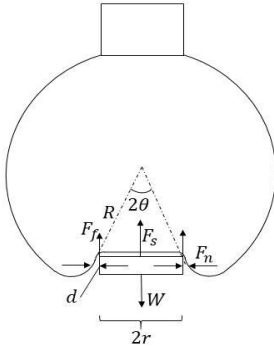


Figure 1 a): Free-body diagram of the gripper lifting a cylinder.

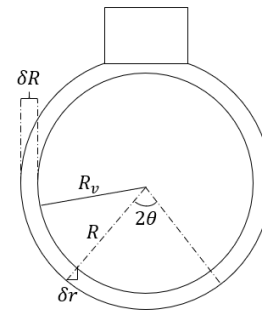


Figure 1 b): Volume change of the gripper moves each point of the sphere a distance of δr in the horizontal direction. The large circle represents the cross-sectional side view of the gripper in its initial configuration and the smaller circle represents the gripper when the air has been evacuated.

As the sphere is evacuated of air, the radius changes by an amount of δR . This results in a decrease in the radius of the horizontal cross-section of the sphere. This is seen in figure 1b as δr . Assuming that the cylinder radius does not change, i.e. the lifted object has a stiffness much larger than that of the granular material. Therefore the normal force that is preventing the contraction can be calculated from the following relationship,

$$\delta r = 0 \Rightarrow \varepsilon_{rr} = 0$$

using Hooke's law:

$$F_N = \frac{\delta r}{r} A_0 E$$

Eq. 1

Slipping occurs when the pressure inside the void between the top face of the cylinder and the membrane is greater than gripping stress at the walls of the cylinder. The following relationship holds:

$$P_v = \frac{F_N}{A_0}$$

Also, the suction force caused by the void is

$$F_s = P_v A_c$$

where A_c is the area of the cylinder top. Now putting these together:

$$F_s = F_f \frac{A_c}{A_0} = F_f \frac{r}{2d}$$

The change in the cross-sectional radius is

$$\delta r = \delta R \sin(\theta)$$

Since the angle θ depends on the height of the cylinder inside the gripper, the total force can be found by summing all the differential force elements along the height of the cylinder. The maximum lifting weight of the gripper is then,

$$W_{\max} = 2\pi\mu E \delta R \int_0^d \frac{r}{\sqrt{(R-h)^2 + r^2}} dh \left(1 + \frac{r}{2d}\right)$$

Where E is the Young's modulus of the granular material, R is the radius of the gripper, r is the radius of the cylindrical object, d is the height of the cylindrical object, h is the differential height element on the cylindrical object, μ is the static friction coefficient and δR is the change of the grippers radius.

The change in radius of the gripper can be written in terms of the volumetric strain:

$$W_{\max} = 2\pi\mu ER \left(1 - \sqrt[3]{1 - \frac{\delta V}{V}}\right) \left(\tan^{-1}\left(\frac{R}{r}\right) - \tan^{-1}\left(\frac{R-d}{r}\right)\right) \left(\frac{1}{r} + \frac{1}{2d}\right)$$

Eq. 2

It can be seen that variables, which can be affected with design of the gripper are the radius of the gripper, volumetric strain and the Young's modulus of the granular material. The volumetric strain is proportional to the pressure difference between the inside and outside of the gripper membrane (bulk modulus). Therefore, a sufficiently powerful vacuum pump is essential for the gripper to provide high gripping forces. The choice of granular material is also essential for the gripper to provide high gripping forces. The granular material must have a sufficiently high Young's modulus, but still be able to compress and deform around various objects.

It should also be noted that the gripping strength depends on the geometry of the gripping object, not only through the contact surface area but also through the contact angle. The contact angle

was assumed to be 90 degrees in these calculations, i.e. the object's contact surface is perpendicular to the ground.

Below is a plot of the maximum lifting capacity for a cylinder with radius of 15 cm and height of 10 cm. Granular material used in the calculation is coffee and the values for the stiffness, friction coefficient and volumetric strain are from previous research [5].

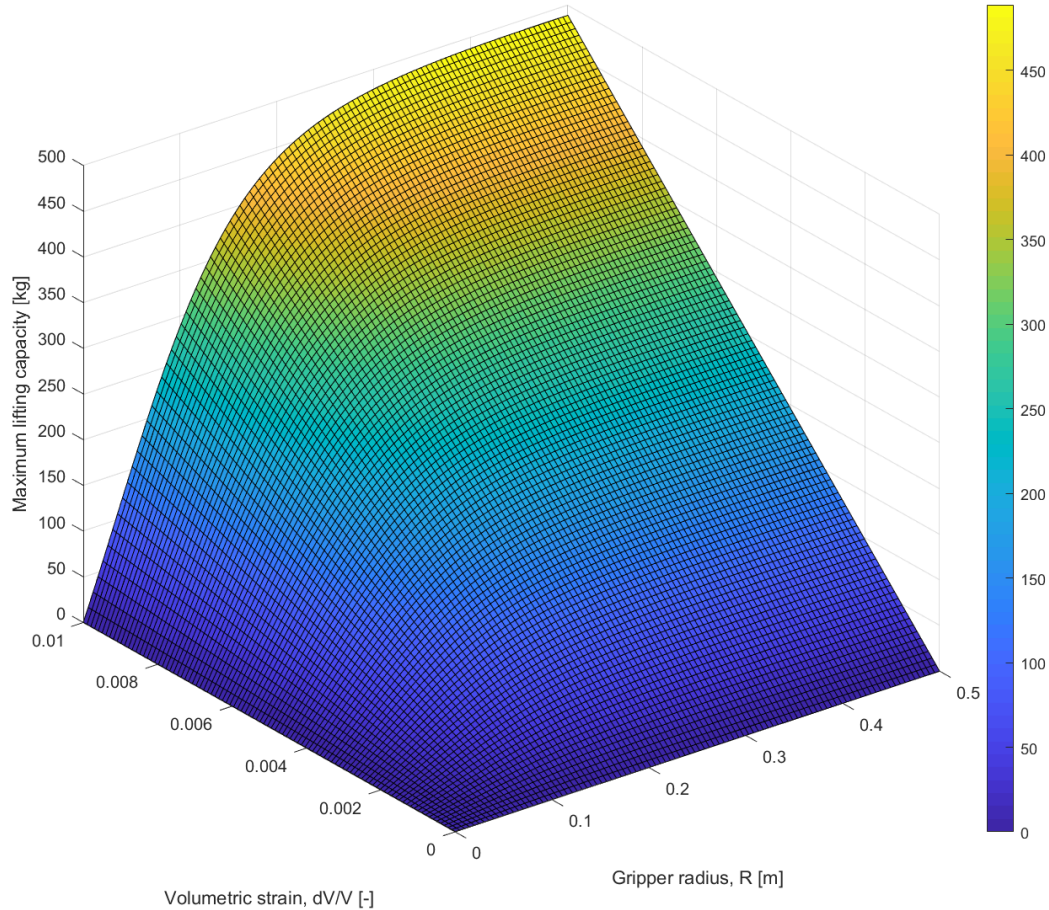


Figure 2: Design variables vs Maximum lifting capacity for cylinder with $r = 0.15$ m and $d = 0.1$ m. The volumetric strain was assumed to be $dV/V = 0.004$ and the gripper radius $R = 0.325$ m. Value for the volumetric strain taken from previous research [5]. Plot produced with MatLab.

Experimental design

In order to gain some knowledge on granule size -parameters effect on the gripping force, wooden pellets were chosen as first material. The second was the same wooden pellets, which were ground to smaller granule size. The wooden pellets were chosen for their relatively advantageous stiffness-lightness ratio. The third granular material used for the study was plastic granules, which were even lighter and stiffer than wooden pellets. The fourth material choice was sand, which has very high stiffness and very high density.

The sheer weight of the granular material inside the grippers pouch can cause great stresses to the surface material. Thus, a custom solution was developed in addition to a typical exercise ball. A ball with an RTV-2 mold silicone coated carbon fiber/glass fiber membrane was developed.



Figure 3 a): Gripper configuration consisting of the following components, 1) the frame body, 2) granular material and 3) the gripper's surface material

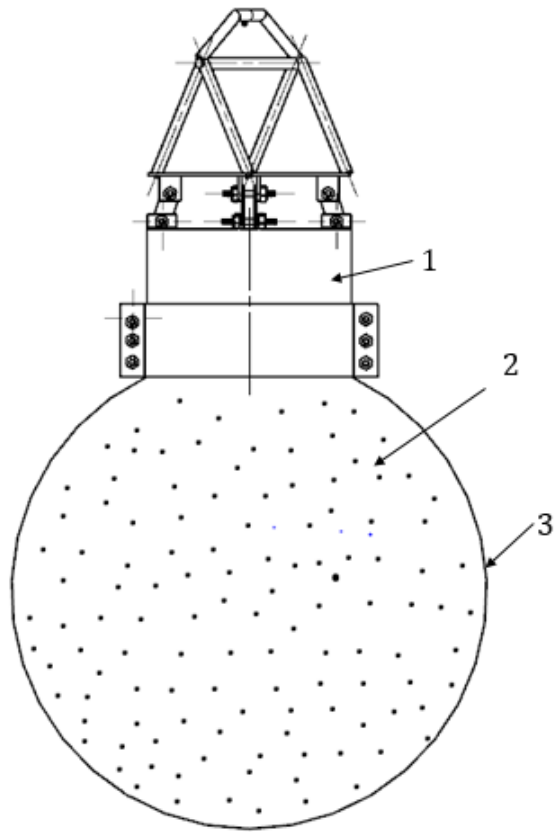


Figure 3 b): Final gripper assembly with vacuum pump mounted on top.

The rest of the system includes a custom rigid structure connecting the pouch with the cranes hook. Also a suction system was connected to the rigid body in order to create a pressure difference between the contents of the membrane and environment. The vacuum machine used was Robinair single stage vacuum pump capable of an ultimate pressure of 0.2 bar. The pump and outlet valve in the frame body were controlled from a smartphone application via bluetooth with an Arduino UNO, a relay and a servo motor. The final setup can be seen in figure 3.



Figure 4: Four different types of granular materials. From the left: sand, ground wooden pellets, plastic granules and wooden pellets.

Table 1. Granular material parameters

Granule material	Granule size	Density	Stiffness
Wooden pellets	Dia = 6mm+-0.2mm Length = 15.6mm+-5mm	696 kg/m ³	1 GPa
Ground wooden pellets	Dia= 6mm+-0.2mm Length 5mm +- 2.5mm	469 kg/m ³	1 GPa
Plastic granules	2.5mm	602 kg/m ³	3 GPa
Sand	0.5mm - 1.5mm	1559 kg/m ³	50 GPa

Table 2. Pouch surface material parameters

reference	Materials	Tensile strength	Elasticity	Thickness	Diameter
Exercise ball 1	PVC	Low	High	1.5 mm	65 cm
Exercise ball 2	PVC	Low	High	1.5 mm	85 cm
Custom ball	Silicon coating, carbon fiber/glass fiber layer.	High	Low	2-4 mm	65 cm

Testing environment

The testing was done with multiple different combinations of granules and membrane surface materials. The combinations are listed below in table 3. Every material combination was put through the same sequence of lifting tasks.

Lifting tasks were performed by placing the lifted object on the ground and lowering the gripper on top of the object. The gripper was lowered until it was no longer hanging from the crane, rather resting on top of the test object. The absolute pressure inside the gripper was lowered to around 0.6 bars using the 0.25 hp vacuum pump.

First task was to lift a 1kg weighing box to make sure the setup is working correctly. Second task was to lift three different shaped objects roughly weighing 5-10 kg: a stool, a trash bin filled with sand and a gym ball. The third lifting task was to lift 30 kg weighing sealed box. The final lifting task was a 120 kg steel cylinder. Test objects, except for the 1kg box, are displayed in figures 5 a)-e). All lifting tasks were rated either as a success or a failure. A task was a success if the membrane could lift the object from the ground and keep it up for 30 seconds. Lifting task could be tried maximum of ten times before it was classified as a failure. One successful lift was enough to classify as a success.

Table 3. Tested material parameter combinations

Combination	Granular material	Pouch surface
1	Wooden pellets	Exercise ball 1
2	Ground wooden pellets	Exercise ball 1
3	Plastic granules	Exercise ball 1
5	Sand	Exercise ball 1
6	Wooden pellets	Exercise ball 2
7	Wooden pellets	Custom ball

Table 4. Test objects and dimensions

Test object no.	Object	Radius	Height	Weight
1	Plastic bucket, standing	10 cm	30 cm	1 kg
2	Stool, standing	32 cm	57 cm (2.5 cm contact area)	5 kg
3	Gym ball	28 cm	-	8 kg
4	Fire extinguisher, laying	15 cm	42 cm	9 kg
5	Trash bin filled with sand and metal weight, standing	27 cm	30 cm	30 kg
6	Steel cylinder, standing	25 cm	35 cm	120 kg



Figure 5 a)-e): Test objects from the left to right are: A stool (not the actual test object in the picture), gymnastic ball, fire extinguisher, trash bin filled with sand and steel cylinder

Results

Tests of the granular materials and membrane materials, where performed according to the previous section. The results of the tests are listed below.

Table 4. Test results for each combination of granular material and gripper surface material

Test object no.	1	2	3	4	5	6
Combination						
Exercise ball 1, wooden pellets	Success	Success	Success	Success	Success	-
Exercise ball 1, ground wooden pellets	Success	Success	Success	Success	Success	Success
Exercise ball 1, POM	Success	Success	Success	Success	Success	Failure
Exercise ball 1, Sand	Success	Success	Failure	Failure	Failure	Failure
Exercise ball 2, wooden pellets	Failure	Success	Failure	Failure	Failure	Failure
Custom ball, wooden pellets	Failure	Success	Failure	Failure	Failure	Failure

The tests made with the exercise ball and the wooden pellets showed promising results. This combination was able complete each task presented. As the results were better than expect a sixth lifting object was added, one that was much heavier than the previous objects. The second test was done with the smaller exercise ball and the ground wooden pellets. This combination proved to be at least equally as good as the previous one. With this combination the granular jamming gripper was also able to lift each of the test objects and also the new 120 kg steel cylinder. The steel cylinder has also a hook protruding from the top face, making lifting even more challenging. The larger exercise ball and the custom ball showed poor performance in lifting, capable of lifting only the 5 kg stool.

When the exercise ball was used as the gripper, two out of the four tested granular material were observed to not be suitable for granular jamming. These were, the plastic granules and the sand. The granular material that performed best was the wooden pellets, which were ground into a fine powder. The second best results were obtained with the exercise ball 1 and wooden pellet combination.

Discussion

Granular materials which compress performed best. As mentioned earlier, the maximum lifting capacity depends on the volumetric strain of the gripper. The volumetric strain increases if the granular material is able to compress into a smaller volume. This results in larger gripping forces and thus a larger maximum lifting capacity. If the material is compressible it also deforms more easily around the geometry of the lifted object. This in turn results in a larger contact surface area between the object and the gripper and thus larger gripping forces.

The granular material which compressed the most out of the tested materials were the ground wooden pellet-material. This is indicated by the large wrinkles forming on top of the gripper surface, when the air was evacuated (fig. 5). The ground wooden pellets -material was also the most suitable granular material for lifting of heavy objects.



Figure 5: Large wrinkles forming on the gripper's surface, when the gripper with ground wooden pellets as granular material was evacuated of air.

While comparing the test results to the analytical solution obtained in section two it has to be remembered that granules were assumed to be similar to ground coffee. The material, which resembles coffee the most is the ground wooden pellet material. This material has a similar granule size and is compressible. Equation 2, gives a maximum lifting capacity of around 270 kg for test object no. 2, which is well above the weight of the heaviest test object. No lifting limit was found to this combination with the current test environment. However, it is highly likely that the maximum

lifting capacity for objects with similar shape as object no. 6 is somewhere very near 120kg. Object no. 6 was successfully lifted only once.

According to equation 2, the gripper lifting capacity is proportional to the gripper radius. A larger radius should give a larger lifting capacity. In the tests the larger exercise ball showed poor performance, as it was only capable of lifting the stool. It should be noted that the tests performed with the larger exercise ball were done with granules filling up only roughly 50% of the ball. The other balls were filled up to around 80%, which is enough to fill up most of the ball and still allow for free movement between the granules before jamming. Further testing with gripper radii should be done to verify the relationship in equation 2.

The results show that granular materials capable of compression perform the best. Out of the compressive granular materials, the one with the smaller granule size performs the best. According to [7], the stiffness of the granular material is larger for smaller grain sizes. These results seem to agree with the test results, since the ground wooden pellets have a significantly smaller grain size than the wooden pellets. The sand granular material had the smallest grain size and, presumably the highest stiffness, but was incompressible and therefore showed poor performance.

Previous work [5] showed that it is possible to use granular jamming to lift objects of various shapes. In this paper was shown that it is possible to use granular jamming in large scale applications, such as overhead crane lifting, to move objects of different sizes and shapes. For a large scale application of the gripper a safety mechanism would have to be designed to prevent slipping of the lifted object. Such a gripper could be used in machine shops or warehouses, where heavy objects of irregular shapes are moved frequently.

References

- [1] D. KIM, W. SINGHOSE, Performance studies of human operators driving double-pendulum bridge cranes. *Control Engineering Practice*, Vol 18 Issue 6, June 2010, pp. 567-576. <https://doi.org/10.1016/j.conengprac.2010.01.011>.
- [2] J. Felip, A. Morales, Robust sensor-based grasp primitive for a three-finger robot hand, *Intelligent Robots and Systems*, (2009) IEE/RSJ International conference 1811-1816, IEEE.
- [3] J. Shintake, V. Cacucciolo, D. Floreano, H. Shea Soft Robotic Grippers, *Advanced Materials*, Vol 34 issue 29, July 19, 2018. <https://doi.org/10.1002/adma.201707035>.
- [4] E. Hawkes, H. Jiang, D. Christensen, A. Han, M. Cutkosky, Grasping Without Squeezing: Design and Modeling of Shear-Activated Grippers, *IEEE Transaction on Robotics* Vol. 34 No 2. April 2018 303-316 IEEE.
- [5] E. Brown, N. Rodenberg, J. Amend, A. Mozeika, E. Steltz, M. Zakin, H. Lipson, H. Jaeger, Universal robotic gripper based on the jamming of granular material, *Proceedings of the National Academy of Sciences* Nov 2 2010 107(44) 18809-18814. <https://doi.org/10.1073/pnas.1003250107>.
- [6] J. Amend, E. Brown, N. Rodenberg, H. Jaeger, H. Lipson, A Positive Pressure Universal Gripper Based on the Jamming of Granular Material, *IEEE Transactions on Robotics*, vol. 28 no. 2341-350 April 2012 <https://doi.org/10.1109/TRO.2011.2171093>.
- [7] J. Amend, Soft Robotics Commercialization: Jamming Grippers from Research to Product, *Soft Robotics* 3(4) 213-222 <https://doi.org/10.1089/soro.2016.0021>.

Integrated car camera system for monitoring inner cabin and outer traffic

Pedrollo Lavinia^{1, a}, Vimpari Jussi^{2, b}, Norema Juho^{3, c}, Fridman Dani^{4, d}, Risto Ojala^{5, e}, Panu Kiviluoma^{6, f} and Petri Kuosmanen^{7, g}

¹University of Trento, Department of Industrial Engineering, Sommarive 9, 38123 Povo TN, Italy

^{2,3,4,5,6,7}Aalto University, Department of Mechanical Engineering, Otakaari 4, 02150 Espoo, Finland

^alavinia.pedrollo@aalto.fi, ^bjussi.a.vimpari@aalto.fi, ^cjuho.norema@aalto.fi, ^ddani.fridman@aalto.fi, ^eristo.ojala@aalto.fi, ^fpanu.kiviluoma@aalto.fi, ^gpetri.kuosmanen@aalto.fi

Keywords: 360 degree camera system, traffic monitoring, car monitoring, motion detection, driver monitoring

Abstract

Camera systems can enhance safety of the vehicles by monitoring traffic in the vicinity, whilst driving. In recent years, research and development in the field of autonomous vehicles has been increasing significantly. Furthermore, installation of a camera system on a vehicle, has provided the researchers with a new platform for traffic monitoring as well as concerns the safety of the animates and surroundings inside and outside the vehicle. In this study, a 360° view camera system is implemented by installing four USB cameras in the exterior bodykit of a Ford Focus 2018, while one is mounted on the rear view mirror from the inside. Moreover, an additional sixth camera has been installed in the interior of the car for monitoring the animates and objects, especially at the backseats. The camera system provides a complete 360° view around the car, leaving no major blindspots, as each camera has been installed discreetly. All the monitored data can be analyzed by an onboard processing device. Although, outcome reciprocate solid foundation, yet further research is required for utilizing the monitored traffic and surveillance of the interiors.

Introduction

Vision-based driver-assistance systems (VBDA) have emerged as a significant contribution for the improvement of Advanced Driver Assistance systems (ADAS), and have had gradually gained a substantial meaning in people's life: every year approximately 1.35 million lives are truncated as a consequence of road traffic crashes. Moreover, between 20 and 50 million people (depending on year and country) undergo non-fatal injuries, including sometimes disabilities as an outcome. [1].

Nowadays car accidents and related deaths represent a daily occurrence because of other's people carelessness (driver's drunkenness, drowsiness, sudden illness), and as several studies show, over 90% of traffic accidents are caused by a human error [1, 2]. However, reliable and consistent machines can be utilized to help humans decrease the aforementioned fatalities.

This project is motivated by the strong willingness of assuring safety and comfort behind the wheel, that concerns both drivers and passengers, and vulnerable road users: pedestrians, cyclists, and motorcyclists.

Driver assistance systems (DAS) have developed from anti-lock braking systems (ABS) in the 80's and Electronic Stability Control (ESC) in the 90's to modern self-parking and collision avoidance systems in the recent decade. In most recent years, these systems have evolved to fully autonomous driving systems, and nowadays every major vehicle manufacturer is developing them. Most of the manufacturers have at least prototypes, while several of them have included some level of autonomous driving even in consumer markets. [3]. In recent decades advanced driver assistance systems (ADAS) have been taken into account as vehicle's detectors, benefitting from computer vision technologies especially in terms of costs: an active sensor - that is, laser or radar sensors - is

way more expensive than an optical one [4]. Especially laser based LiDARs (Light Detection and Ranging) have been popular in autonomous driving solutions, due to their efficiency and high accuracy, but because of their price, some manufacturers see purely optical sensors as a more viable solution [5].

This paper covers designing, developing and manufacturing a smart camera system for a Ford Focus 2018 that is able to monitor both outer and inner conditions. Development includes researching the topic to design and producing consequently a competent solution for a camera system that is a consumer level product: mountings and wiring are implied to car's original wiring in the best way possible. The system comprises an onboard computer, which is located in the trunk and cabling is accomplished in a way that all the cameras are plugged in by means of individual universal cables. Early solutions in 360° camera systems in [6] and [7] depict the general guideline for the placement of four outer cameras: two of them are attached to the side mirrors, one is fixed to the frontal bumper or dashboard, and one is located in the back for rear view. Although this project does not provide a driver monitoring system, the auxilium of one camera added to the front inner cabin of the vehicle could serve for machine vision detection methods, as presented in [8], [9] and [10]. These detections especially focuses on drivers' eyes surveilling, because it's most easily detected and most consistent sign of human's tiredness.

Methods

The purpose of this camera system is to provide a 360° surround outer view and an inner monitoring of the cabin's backseats and back footwells. It has been tested on a Ford Focus 2018, even though it is applicable to any vehicle. First task was deciding which combination between positioning, angle, number and type of camera would have been the most suitable in terms of costs, efficiency, data processing and blind spots minimization. Primary tests were carried by means of a cheap action camera with fixed view angle of 120°, easily affordable from cameras currently in the market.

The car was driven to a suitable open wide place to take snapshots from the camera's images with the purpose of measuring possible angles for each camera. A computer was used to monitor the camera views through the application provided by the camera's company itself. It was noticed that the front view presented negligible blind spot areas. In fact, the optimal angle of view created by a fixed focus camera there, leaves unmonitored a reasonably small area close to the front bumper. The practical tests proved that the 120° cameras could perform a feasible outer surveillance. However, this could be achieved only with a chosen optimal configuration, consequently, cameras with the same angle of view were chosen for the vehicle's outside. The same testing demonstrated that a 120° camera was not enough to monitor the backseats and the back footwells, thus requiring the purchase of a wide-angle camera.

An on-board computer was installed inside the car's trunk to collect and process the information gathered by the cameras. Therefore USB cameras were chosen as the main camera type: thanks to the "plug-and-play" system, the combination of multiple USB connections provide enough power and transfer data simultaneously by means of the easiest way of camera connection (wireless cameras for instance would have lead to huger data transfer and image acquisition problems due to the inefficiency of this method with multiple cameras). Furthermore, small size of the cameras and 720p (HD) video with 30 FPS (Frames Per Second) were set as requirements for the cameras.

Results

The best solution found in terms of number of cameras (and consequently cost), data processing and blind spots minimization for the outer monitoring consists on five cameras:

- One ELP 720p 120° usb camera mounted on rear view mirror from the inside (Figure 1).
- Two ELP 720p 120° usb cameras mounted on side mirrors (Figure 2).
- Two ELP 720p 120° usb cameras mounted on rear window trim (Figure 3).

Each camera's casing was 3D-printed after a proper design work. Measurements in situ were first accomplished by means of a digital caliber and a SolidEdge model was drawn consequently. These designs allow the cases to fit in car's parts specific shapes in order to make cameras less visible, and to give the system a more appreciable look.

Fig. 1 displays the front view camera which was located inside the car in proximity of the rear view mirror in order to make sure that front view is not affected by the weather conditions (e.g. snow), dirt and dust, that might obscure the lens. This setup assures a clean view, eventually counting on the aid of windshield wipers and heated glass of the car's front window. Fig. 2 and Fig.3 show camera casings in the side view mirrors and rear window trim. As later illustrated in Fig. 5, the outer cameras provide an exhaustive 360° making blind spots negligible. These are such small that, according to practical tests, pedestrians are seen at least partly by the cameras, even though they are standing in one of the mentioned blind spots. Camera casings in the outside of the car are also made weatherproof by adding fixed clear polycarbonate lenses, rubber sealings between casing backplates, and proper rubber grommets for the cables.

For the interior condition monitoring, one ELP Aptima 5Mp 170° usb camera was installed into the side headlining to replace the dorm light in Fig. 4. Its wide angle feature permits to cover the whole back seat and legroom. The original circuit board of the dorm light was fitted inside the 3D-printed casing, and the new button (acting as a light switch) was manufactured from aluminium by using lathe. This allowed the dorm light and its functions (such as dimming and proper on/off switch) working as intended by the car's manufacturer, therefore providing the different casing as the only changes of the initial dorm light configuration.



Figure 1. Front casing



Figure 2. Side view mirror casings.



Figure 3. Rear window trim casings.



Figure 4. Interior casing in side headlining.

Fig.5 illustrates viewing angles, positions and cablings of the cameras. On its left, an outer overview of the 360° system is given by means of yellow shaded 120° angle cones departing from the cameras' sites. On the right the cabling schematics is depicted, task accomplished through car's own cabling routes: cables are routed through car's original grommets and tunnels, so that each cable is properly sealed and hidden. This provides an aesthetically pleasing design to whole camera system. Table 1 follows, labelling the cameras symbolized in Fig.5 by means of numbers.

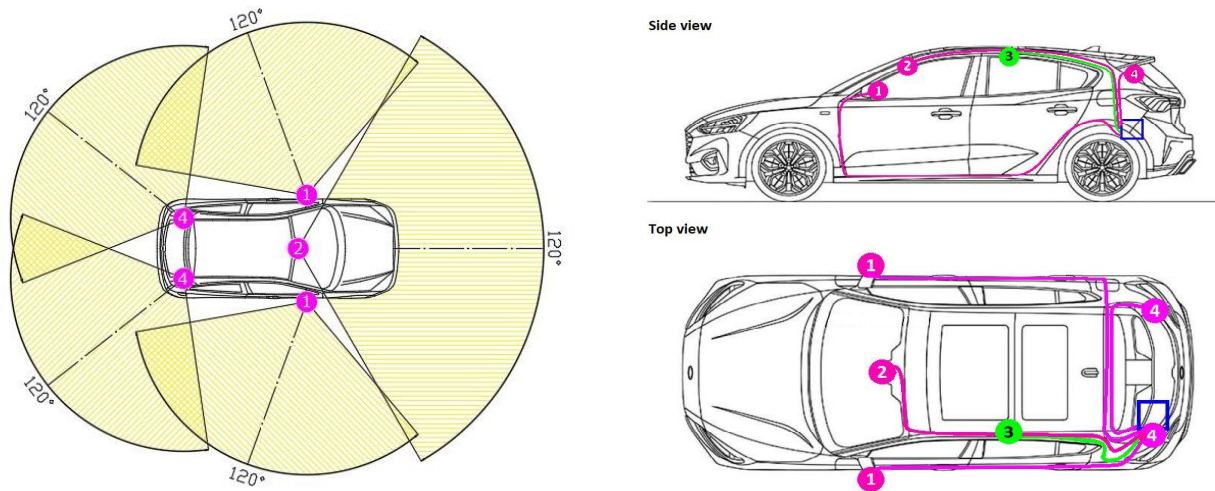


Figure 5. Viewing angles, positions and cablings of the cameras.

Table 1. Labels in figure 5.

Label number	Camera	Location
1	Two ELP 720p 120° usb cameras	Side mirrors
2	Two ELP 720p 120° usb cameras	Rearview mirror
3	One ELP Aptima 5Mp 170° usb camera	Side headlining
4	Two ELP 720p 120° usb cameras	Rear window trim

A real view of the working camera system tested in a traffic situation can be seen below in Fig. 6 and Fig. 7. The panoramic view is splitted in half in order to make view more visible in paper format. As clearly stated by the figures, the whole 360° of the outside is covered, noticing that same vehicles and objects can be seen simultaneously in consecutive images. The latter half image of Fig.6 and the former of Fig.7 if combined give a full 360° panoramic view.



Figure 6. Left side view of the cameras.



Figure 7. Right side view of the cameras.

Summary

Both aims of providing a 360° outer view and an inner monitoring of the cabin's backseats and back footwells were achieved and proved by driving tests of the car model Ford Focus 2018. The system not only acquires images all around the vehicle, but also permits their memorization to be exploited for research purposes. The installation of the interior camera for the backseat monitoring revealed to be a successful task as well, both providing the wanted whole back cabin view and being matching designed for the car's interiors. Chosen locations for the cameras in addition with cables installed from camera units to the trunk of the car do provide an easy and user-friendly use of the camera system without noticeable delays or distortions.

For future research the outside camera system can be exploited for several kinds of purposes ranging from machine vision testing to road condition monitoring and internet of things appliances. The interior camera allows the research to continue, for instance to accomplish the surveillance of automated taxis and rental cars. Some of these appliances have already been tested with the system developed. Video recordings gathered during a driving test were used by YOLOv3 machine vision software with good results, clearly recognizing distinct objects, people, vehicles in the car's surroundings. The interior camera was utilized for research by means of a CAN-bus of the car with the aim of giving signals to a computer that exploits the camera for backseat condition monitoring.

References

- [1] World Health Organization. (2018). Road traffic injuries. [online] Available at: <https://www.who.int/news-room/fact-sheets/detail/road-traffic-injuries>.
- [2] Singh, S. (2015, February). Critical reasons for crashes investigated in the National Motor Vehicle Crash Causation Survey. (Traffic Safety Facts Crash•Stats. Report No. DOT HS 812 115). Washington, DC: National Highway Traffic Safety Administration. Available at: <https://crashstats.nhtsa.dot.gov/Api/Public/ViewPublication/812115>.
- [3] Bengler, K., Dietmayer, K., Färber, B., Mauer, M., Stiller, C. and Winner, H. (2014). Three Decades of Driver Assistance Systems: Review and Future Perspectives. [online]. Volume 6(4), pp. 622. Available at: 10.1109/MITS.2014.2336271.
- [4] Ying-Che, K., Neng-Sheng, P. and Yen-Feng, L. (2011). Vision-based vehicle detection for a driver assistance system. Computers & Mathematics with Applications, volume 61(8), pp. 2096-2100. [online]. Available at: 10.1016/j.camwa.2010.08.081.
- [5] Hawkins, A. (2018). Elon Musk still doesn't think LIDAR is necessary for fully driverless cars. The Verge. Journal. [online]. Available at: <https://www.theverge.com/2018/2/7/16988628/elon-musk-lidar-self-driving-car-tesla>. [Accessed 3.2.2019].
- [6] Mazzilli J.J. (2005). US 2005/0140785 A1.
- [7] Schofield, et al. (2003). US 6,611,202 B2.

- [8] Klette, R. (2015). Vision-based Driver Assistance Systems. [online]. Available at: 10.13140/2.1.2498.6404.
- [9] Velez, G., Otaegui, O., Ortegam J., Nieto, M. and Cortes, A. (2015). On creating vision-based advanced driver assistance systems. Intelligent Transport Systems, Volume 9(1), pp. 59-66. [online]. Available at: 10.1049/iet-its.2013.0167.
- [10] Simic', A., Kocic', O., Bjelica, M. and Milosevic', M. (2016). Driver monitoring algorithm for advanced driver assistance systems. Telecommunications Forum, Belgrade, Serbia. [online]. Available at: 10.1109/TELFOR.2016.7818908.

Inverted pendulum controlled with CNC control system

Henry Konnos^a, Topias Tyni^b, Aishwarya Dharamsi^c, Panu Kiviluoma^d and Petri Kuosmanen^e

Department of Mechanical Engineering, Aalto University, Finland

^ahenry.konnos@aalto.fi, ^btopias.tyni@aalto.fi, ^caishwarya.dharamsi@aalto.fi,

^dpanu.kivluoma@aalto.fi, ^epetri.kuosmanen@aalto.fi

Keywords: Linear motor, Inverted pendulum, Sinumerik, G-Code

Abstract

CNC control system are widely used for machine tools and other production machine applications. Typical program of machine tools or production machines defines line by line instructions stating position of the axis. Normally feedback control loops are not used. In this study the performance of the CNC control system performance was tested in an application of inverted pendulum actuated with linear motor. As a result, the control system stabilized the inverted pendulum successfully. It could also stabilize itself in few seconds after external disturbance. The built system could be useful for research and educational institutions for teaching purposes.

Introduction

Inverted pendulum is a classical testing application for the different control systems and methods. Without control the inverted pendulum is unstable and it will fall from its upward position. Inverted pendulums are usually implemented with cart, belt, rotating DC motor and with simple microcontroller control, for example.[1] Depending on the system used and its dimensions, the response is different. However, working control for the inverted pendulum could stabilize the pendulum in less than 2 seconds, when magnitude of disturbance is around 20 degrees [2].

Siemens Sinumerik 840d sl CNC control system is widely used for machine tools and other production machine applications, such as laser machining and handling systems [3]. Typical program of machine tools or production machines defines line by line instructions stating position of the axis for the upcoming state and what is the movement like during the motion [4]. Typically, g-code programs don't use feedback control loops in it. Our goal was to test something with this system where it is not usually used for. Therefore, to test the performance of the Siemens CNC control system, an inverted pendulum was implemented with it.

In this research project, Siemens Simotics L-1FN3 linear motor is used to move the pendulum. Typical fields of applications for this type of linear motor is high-performance machine tools and production machines [5]. Linear motor is optimal component for the inverted pendulum. The pendulum needs precise and fast control and those are advantages of linear

motors compared to other solutions. With linear motor the set-up of the system is also more robust, because of fewer amount of moving parts involved in it.

The application could be for demonstrating the capabilities of the Siemens' technologies. Also this research would help explore the applicability of G-codes for intelligent self-stabilizing ability of the linear motor. This could be useful for research and educational institutions for teaching purposes.

System description of inverted pendulum

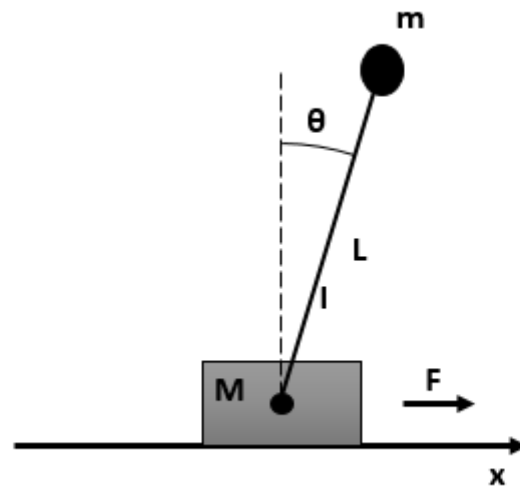


Figure 1. Model of inverted pendulum.

M: Mass of the linear motor's carriage

m: Mass point in pendulum's top

x: Position of the carriage

θ : Angle of the pendulum

I: Inertia of the pendulum

L: Length of the pendulum

F: Force from the motor

Mechanical design of the pendulum is illustrated in figure 2. The bracket is made of aluminum and it is attached by bolts to the motor's carriage. There is servo motor on the top of the bracket, which is disabled. The pendulum uses the motor's axis as rotation axis and the control system gets the angle data of the pendulum from the motor's encoder. The friction of the motor is small enough that it is not affecting to the control substantially. The pendulum is made of wood and it is 700 mm long. The mass of the pendulum is 0.5 kg and the carriage with the bracket has mass about 9 kg.

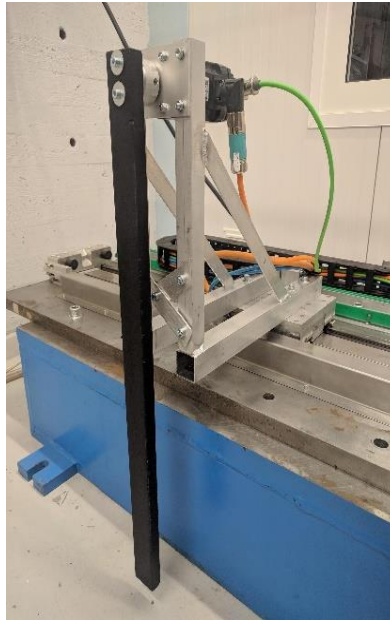


Figure 2. Mechanical design of the inverted pendulum.

Sinumerik 840D sl is an industry standard for CNC machines' control system. It's capable to controlling 93 axes and up to 30 machining channels. In our application it is used to control the Simotics linear motor and the encoder data is also handled via the Sinumerik 840D sl. G-code is used to control the linear motor and eventually stabilizing the pendulum.

Simotics L-FN3 linear motor has all features that are needed for stabilizing the pendulum (Table 1). Its maximum acceleration and velocity are high enough for the system of the project. Accuracy and precision are the key features of this linear motor and those are important for the successful control. The range of the linear motor's movement is limited by software to 800 mm in this project.

Table 1. Features of the linear motor

Max. velocity	3.66 m/s
Max. acceleration	27 m/s ²
Max. force produced	600N

Control

PID algorithm is used to calculate the control value. The system has one PID for controlling the angle of the pendulum, which get the feedback signal from the encoder of the pendulum's axis. Another PD is for controlling the position of the carriage, which get the feedback signal from the linear encoder. The output value of the whole control loop is velocity of the motor. The scheme of the feedback control loop can be seen in figure 3. The controllers are tuned with trial and error method.

In the start of the program, the swing-up function swings the pendulum to upright position. The swing-up function is implemented with synchronous action of the system. The function is driving the motor to four points and that makes the pendulum swing up. When the pendulum

is close enough the upright position, the control loop starts, which calculates the control value. The loop uses system's R variables to its calculations. The loop constantly updates the control value, which is used in synchronous action commands. The synchronous actions set the direction and the velocity for the motor according to the R control variable.

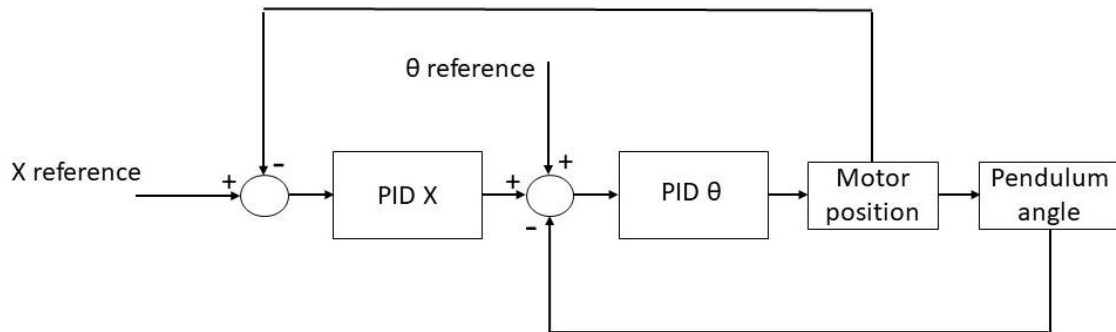


Figure 3. Control loop diagram.

Results

As a result of this project, the pendulum is stabilized successfully by Siemens' control system and linear motor. Figures below show behavior of the system, when reference angle is 180 degrees and reference point in x-axis is 550 mm.

Firstly, the pendulum is in upright position and it is hit with other rod at 0.4 second. As it can be seen in figure 4, the control starts to fix the error immediately and the angle of the pendulum does not grow large. The largest error in angle occurs, when the motor turns its direction first time and it is furthest from its reference point (Figure 5). Before four seconds have passed from the disturbance, the pendulum is stabilized and it is close to its x-axis reference point.

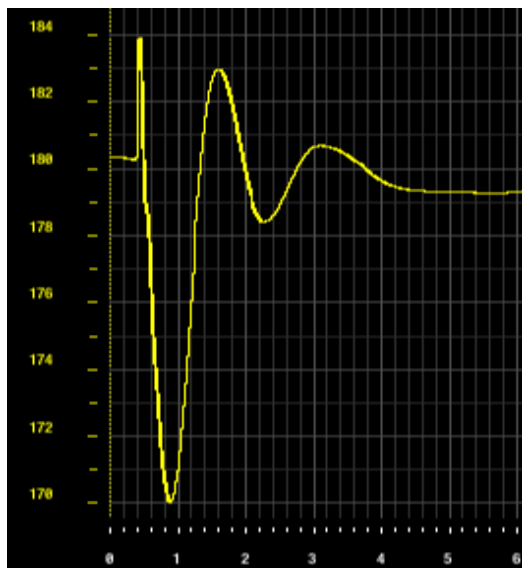


Figure 4. Angle of the pendulum.

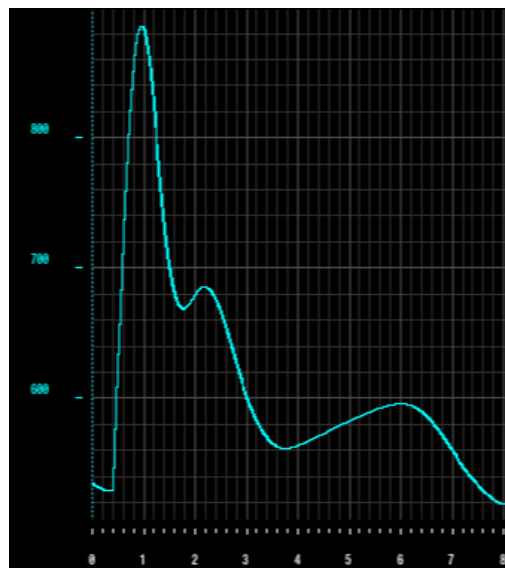


Figure 5. Position in x-axis.

When the pendulum is stabilized, the angle varies between 179.5 and 180.5 degrees. The position of the motor in x-axis varies relatively more than angle, when the carriage moves between 500 and 600 mm. Spending more time tuning the control values of the controller should decrease swinging of the carriage.

Discussion

In this study, it was noticed that some of the commands cause significant amount of delay to the program. Reading sensor data in the middle of the loop made the program slow, for example. This problem was fixed so that sensor data was saved to the R-variable in synchronous actions and that R-variable was used in the control loop. Also reading and saving values of R-variables to the file was tried in the loop, but it made the loop operate extremely slow. Only small amount of time was used for that problem and any solutions for that wasn't discovered.

Also in the swing-up function delays of the system was affecting to the behavior of the pendulum. First it was tried to swing the pendulum up with basic G-code commands. Those commands would have function, if the delays between different movements had been similar everytime. But with same parameters, the same stops, when the motor changed its direction, lasted different amount of time. It was impossible to get the swing-up function work properly. This problem was also fixed with synchronous action. With those commands the movement was more identical everytime. The temperature of the motor and the system affected slightly to the behavior of the swing-up. When the program was driven with cold system, the swing-up function swung the pendulum a little short of the reference point and the upright position. But when the motor was driven constantly and temperature rose, the swing up function swung the pendulum a little over of the upright position.

It is sure that spending more time of tuning PID control values, the control could stabilize the pendulum quicker and be more robust. Also the velocity and the accuracy of the systems seem so good that the double inverted pendulum could be implemented with it. However, that would need some sort of model-based controller. In the model of the inverted pendulum the output is usually force in the x-direction. And in this system the output was velocity of the motor. That created a challenge, which wasn't solved in this project.

References

- [1] Wiki Aalto. Mechatronics Exercise. Projects 2014.
<https://wiki.aalto.fi/display/MEX/Inverted+Pendulum>
- [2] Stabilization of Real Inverted Pendulum Using Pole Separation Factor. Proceedings of 2012 International Conference on Mechanical Engineering and Material Science (MEMS 2012). 2012. Amr A. Roshdy, Yu zheng Lin, Hany F. Mokbel, Tongyu Wang.
- [3] Siemens. Products and Services. Industrial Automation Sinumerik CNC automation system. CNC-Systems. Sinumerik 840.

<https://new.siemens.com/global/en/products/automation/systems/cnc-sinumerik/automation-systems/sinumerik-840.html>

[4] Autodesk. Industry. Manufacturing. Resources. Manufacturing-engineer. G-code. <https://www.autodesk.com/industry/manufacturing/resources/manufacturing-engineer/g-code>

[5] Siemens. Drive technology. Motors. Motion Control Motors. Simotics L Linear Motors. Simotics L-1FN3 Linear motors. <https://w3.siemens.com/mcms/mc-solutions/en/motors/motion-control-motors/simotics-l-linear-motor/linear-motors-1fn3/Pages/linear-motors-1fn3.asp>

Multi-material mixer and extruder for 3D printing

Jimi Lehtola^a, Pradeep Tajhya^b, Oliver Tallavaara^c, Arturo Pellicer^d, Ashish Mohite^e, Panu Kiviluoma^f and Petri Kuosmanen^g

Department of Mechanical Engineering, Aalto University, Finland

^ajimi.lehtola@aalto.fi*, ^bpradeep.tajhya@aalto.fi, ^coliver.tallavaara@aalto.fi,
^darturo.pellicermaseres@aalto.fi, ^eashish.mohite@aalto.fi, ^fpanu.kiviluoma@aalto.fi,
^gpetri.kuosmanen@aalto.fi

Keywords: epoxy, additive manufacturing, industrial robot, printing

Abstract

This paper describes the building of a functional multi-material extrusion machine that allows printing on a large scale using non-conventional materials. 6-axis Industrial robot was utilized as a platform for 3D printing and the extrusion system was built separately. The study focuses on the control system for mixing and extruding multi-materials with the robot, thus leaving the chemistry discussion of two-component materials to a minimal side. Results show that mixing and extruding high viscous two-component material is possible but making complex multi-layer shapes using liquid materials need further research and development. It is possible to implement an extrusion system to an existing product such as KUKA robot. The PLC systems modularity and expandability offers many solutions for future upgrades such as mentioned in future improvements section.

Introduction

The availability of different scale printers and a wide selection of materials offer great benefits for rapid prototyping and creating models that were previously impossible to manufacture using traditional manufacturing methods. 3D printing as an additive manufacturing process, making objects from 3D model data [1], was strongly established with the use of plastic materials in the form of solid filament windings, known as Fused Filament Fabrication (FFF) [2]. There is a large knowledge base collected on the mechanical properties of the most common filaments used [3]. The tensile strength and elastic modulus of printed components using realistic environmental conditions for a selection of open-source 3D printers find an average tensile strength of 28.5 MPa for ABS and 56.6 MPa for PLA with average elastic moduli of 1807 MPa for ABS and 3368 MPa for PLA [4].

As of July 2018, the most used 3D printing method is by far the FFF (also known as FDM) with a share of 69 percent. This is then followed by Stereolithography & Digital light processing, Selective laser sintering, Material Jetting and Metal Sintering [7]. However, a new additive method emerges with great present and future projection. This 3D printing method is called multi-material extrusion and is currently applied for different purposes such as tissue engineering/ multi-colored surgical parts in the medical field, reducing environmental impact on pollution [8]. One example is the printing of epoxy structures that have fiber as reinforcement. Young's modulus of these materials exceeds up to 10 times higher values compared using commercially available 3D-printed polymers, while maintaining comparable strength values [5]. Two-component materials combined with complex geometry enabled by 3D printing offer great mechanical properties and reduced weight of the product against components that are made by using traditional manufacturing methods [6].

While the conventional extrusion-based 3D printing involves melting of solid material for extrusion, this project is focused on creating a system for extrusion and mixing of two viscous material(s) without an external heat source, which is the most common way of curing epoxies [10]. These materials are suitable for 3D printing because of high adhesion strength and good processability. The uncured epoxy resins have poor mechanical, chemical and heat resistance; by reacting the linear epoxy resin with suitable curatives, three-dimensional cross-linked thermoset

structures can be obtained. This is ideal for the mechanical and thermal properties, resulting in high modulus, failure strength and great bonding for many industrial applications [11].

This study is focused on multi-material extrusion involving Epoxy, field which is not very widely developed and offers great opportunities. The method used is going to utilize two components consisting of hardener and (Epoxy) resin, which are mixed together, and then cured by the chemical reaction [9]. Since this process is going under development, this project will aid in the further development of this type of layered manufacturing.

System description

Extruding two different materials need a plunging mechanism and mixing them before extrusion. The control system includes a linear actuator, plunging pistons, cartridges with metal supports, fittings, tubes, mixing head and static mixer as seen in figures 1 and 2. The two materials were filled separately in the two 177cc cartridges and then plunged to the mixing head through tubes using the linear actuator, keeping the materials separated before the mixing head. The linear actuator had a stroke length of 200 mm and maximum dynamic force of 1000 N. The materials were then mixed in the static mixer through which the extruded material came out.

This system does not allow to change cartridges during printing. So, the size of the cartridge restricts the size of the printable object. The plunging system was modular designed, for it to be used for different lengths of cartridges. Increasing the stroke length of actuator and the length of the plunger allows to increase material volume through longer cartridges. The speed of the actuator movement was controlled to have the desired rate of extrusion of the materials. To avoid the additional weight on the robot arm, the plunging system was mounted on an aluminum stock profile. This location further allowed the variability option of the cartridge length depending on the need of the printing size.



Figure 1 Extruding system: 1. Linear actuator, 2. Pistons, 3. Cartridges with metal cylinders, 4. Stainless steel fitting and brass adapter, 5. Nylon tubing

Table 1 Main components of the system

S.N.	Component ID	Description	Specification	Qty
1	DLA-24-40-A-200-POT-IP65	Linear actuator	24 V, 200mm stroke length, 1000N dynamic force	1
2	Mixer	Casted aluminum mixer	2x 1/4 thread into bayonet nozzle attachment	1
3	TS60CWP	Cartridges	(PP) 177cc	2
4	BAE PS-XA-1W-24-050-003	Power supply converter	115/230 VAC 2.8/1.4 A 47-63 Hz	1
5	EK1100	EtherCAD Coupler	Power contacts: max. 24 V DC/max. 10 A	1
6	EL7342	DC motor Driver	Max current: 2 x 3.5 A	1

The cartridges were intended for single use only. Once pistons are fully pressed in, the cartridges must be manually removed and replaced again for the next print. This means that their placement and removal from the structure is a process that will take place often, so an easy access and a simple replacement solution were provided. Two 3D printed supports were created to have both cartridges in horizontal position next to each other. The support located in the rounded heads of the cartridges, where the material will be extruded, was designed in order to act as stopper support and have enough rigidity to withstand the forces created during the plunging movement. This was done to prevent the cartridges from moving or misaligning. In addition, metal cylinders were used to strengthen the plastic cartridges, which at first started to deform under the pressure in the system without them and cause leakage.

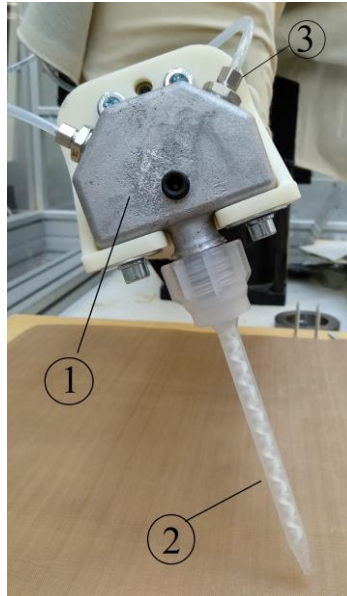


Figure 2 Mixing interface: 1. Mixing head, 2. Static mixer, 3. Stainless steel fitting

Brass fittings with NPT and BSPT threads were used as adapters between plastic cartridges and stainless-steel fittings. Red translucent nylon tubing with an inner diameter of 4 mm was used for feeding the material at the tip of the robot arm due it being flexible and resistive to most chemicals. On the sixth axis of the KUKA robot, the mixer was mounted into a quick release mount. The mixer allows for two material feeds to be joined and initialize the chemical reaction between the hardener and the resin. Mixing was further aided by using replaceable static mixers with 15 mixing elements inside, which helps the flowing material to blend together while flowing towards the tip. The mixer was made to be removable and resistant to chemicals, allowing to clean it with solvents after each print. To aid the cleaning at the contact point of two materials inside the mixer, a check hatch was implemented into the section where the resin and the hardener start to blend together.

Control system implementation and parameters

A 6-axis KUKA robot was used as a platform for the 3D printing. An EK1100 PLC system from Beckhoff was utilized as a building base for the extrusion control (Figure 3). A 24 V DC converter was used to power the drives. EL7342 DC motor controller output pins for motor A were programmed with KUKA's Workvisual software as digital output pins. Digital output 38 was set to toggle the command to activate the motor on and off, pins 39-54 were mapped to control the velocity of the linear actuator's DC motor as a binary value, where output 54 enables the reversion of the DC motor. For driving the DC motor at wanted speed, the digital outputs 41,43,47,48 and 52 were enabled. Toggling these values gave empirically slowest speed setting for the DC motor.



Figure 4 First layer print with ARALDITE 2012 A/B

Future improvements

For easier cleaning system, the aluminum mixer should be re-designed so that the mixing point would be at the very tip of the casting. Optionally a third line could be inserted into the aluminum casting, where a stream of solvent would be plunged through the mixing head to automate the cleaning after printing.

To automate the printing and have repeatable results, a pressure sensing feedback loop could be utilized to control the DC motor speed with different materials. This would require having a pressure sensor at the tip of the cartridges, giving a signal back to PLC and then suitable DC motor speed could be adjusted within the running code to achieve some pressure.

Large scale printing would benefit from a distance sensor which would measure the actual layer height of the print and make a comparison with what it should be in the code. If the material is quite liquid or the curing time is long, it is most likely that the print will collapse once it settles down. The same could happen only due to the mass of the print when printing larger scale models.

The printing of ARALDITE 2012 A/B was done with 1:1 ratio. When mixing with different ratios, a secondary motor could be added to drive the other cartridge piston. This could be done by adding the other motor to an existing PLC system that has an output for the second motor.

References

- [1] ISO/ASTM 52900. (2017). Additive manufacturing. General principles. Terminology. Geneva, Switzerland: International organization for standardization. 19 p
- [2] M. Mohseni, D.W. Hutmacher, N.J. Castro, (2018), Independent evaluation of medical grade bioresorbable filaments for fused deposition modelling/fused filament fabrication of tissue engineered constructs, *Polymers (Basel)* 10
DOI: 10.3390/polym10010040
- [3] Nagendra G. Tanikellaa, Ben Wittbrodtb, Joshua M. Pearce. (2017). Tensile strength of commercial polymer materials for fused filament fabrication 3D printing.
DOI: 10.1016/j.addma.2017.03.005
- [4] B.M. Tymrak, M. Kreiger, J.M. Pearce, (2014) Mechanical properties of components fabricated with open-source 3-D printers under realistic environmental conditions, *Mater. Des.* 58 242–246.
DOI: 10.1002/adma.201401804.

- [5] Compton, B.G., Lewis, J.A. (2014). 3D-printing of lightweight cellular composites. *Advanced Materials*, 26 (34), pp. 5930-5935.
- [6] G.B. Odom, Morgan & B. Sweeney, Charles & Parviz, Dorsa & P. Sill, Linnea & A. Saed, Mohammad & J. Green, Micah. (2017). Rapid curing and additive manufacturing of thermoset systems using scanning microwave heating of carbon nanotube/epoxy composites. *Carbon*. DOI:120.10.1016/j.carbon.2017.05.063
- [7] Statista (quoted 3.2.2019), Worldwide most used 3D printing technologies, as of July 2018. <https://www.statista.com/statistics/756690/worldwide-most-used-3d-printing-technologies/>
- [8] Pedersen, David Bue. (2013) Additive Manufacturing: Multi Material Processing and Part Quality Control
http://orbit.dtu.dk/files/77749134/V2_lille_phd_afhandling_David_Bue_Pedersen..PDF
- [9] K. Formela, Ł. Zedler, A. Hejna, A. Tercjak. (2017). Reactive extrusion of bio-based polymer blends and composites – Current trends and future developments.
DOI: 10.314/expresspolymlett.2018.4
- [10] G.B. Odom, Morgan & B. Sweeney, Charles & Parviz, Dorsa & P. Sill, Linnea & A. Saed, Mohammad & J. Green, Micah. (2017). Rapid curing and additive manufacturing of thermoset systems using scanning microwave heating of carbon nanotube/epoxy composites. *Carbon*. DOI:120.10.1016/j.carbon.2017.05.063
- [11] Domun, N., Hadavinia, H., Zhang, T., Sainsbury, T., Liaghat, G. H., Vahid, S. (2015) Improving the fracture toughness and the strength of epoxy using nanomaterials – a review of the current status <https://pubs.rsc.org/en/Content/ArticleLanding/2015/NR/C5NR01354B#!divAbstract>

Object detection and trajectory planning using a LIDAR for an automated overhead crane

Sampo Simolin^{1,a}, Kaarle Patonmaki^{1,b}, Arnab Chattopadhyay^{1,c}, Joakim Högnäsbacka^{2,d}, Mikko Lähteenmäki^{2,e}, Joonas Pulkkinen^{2,f}, Janne Salovaara^{2,g}, Timo Oksanen^{2,h}, Panu Kiviluoma^{1,i} ja Petri Kuosmanen^{1,j}

¹Department of Mechanical Engineering, Aalto University, Espoo, Finland

²Department of Electrical Engineering and Automation, Aalto University, Espoo, Finland

^asampo.simolin@aalto.fi, ^bkaarle.patonmaki@aalto.fi, ^carnab.chattopadhyay@aalto.fi,
^djoakim.hognasbacka@aalto.fi, ^emikko.lahtenmaki@aalto.fi, ^fjoonas.pulkkinen@aalto.fi,
^gjanne.2.salovaara@aalto.fi, ^htimo.oksanen@aalto.fi, ⁱpanu.kiviluoma@aalto.fi,
^jpetri.kuosmanen@aalto.fi

Keywords: autonomous system, obstacle avoidance, machine vision, material handling

Abstract

Overhead cranes are used widely in industry for cargo handling. This study demonstrated the use of LIDAR for autonomous navigation of an overhead crane in a warehouse environment. This proposed crane system decides its path solely based on the LIDAR sensor data. First the LIDAR rotates 360 degree to generate the environmental map data and based on it, it determines the trajectory to the final coordinate chosen. The map is dynamically updated as the crane autonomously navigates through the surroundings. This system was put through some navigational tests and scenarios in the warehouse and it successfully demonstrated the concept.

Introduction

Overhead cranes are used widely in industry for cargo handling. They are usually being handled by an operator, who has a controller to move the crane. Handling an overhead crane can potentially be dangerous for surrounding people without proper precautions, and even with high safety regulations accidents do happen. Cargo handling as a business has tight business margins, and every way of improving the economic efficiency is welcome to the business.

This study is focusing on those aspects of overhead cranes: improving safety and the efficiency of cargo handling with an overhead crane. This is done by studying the possibilities of making an overhead crane autonomous. There has been research on autonomous crane operation already in warehouse and other environments [1, 2, 3]. These articles describe methods for collision detection and trajectory planning. In this study, however, a LIDAR (light detection and ranging) is used as the main tool for the automation to achieve excellent reliability, efficiency and safety with heuristic and dynamic self-control by the crane. Laser scanners have been previously used for improving visibility of the crane operator [4, 5] and also for other path-planning applications, including UAVs [6], but there is only a little research about providing data of the environment for autonomous crane operation. Research on using point cloud and building a 3D map of the environment has been done, and it is applied to this study [7]. Also, there

is a lot of research done on trajectory planning, and there should be enough information and algorithms to make this part of the project work even in uncertain situations [8,9]. Path planning is possible to apply even in dynamic situations, where environment changes [10].

Methods

System contains an overhead bridge crane, whose hardware capabilities are listed in Table 1. The crane can be moved by providing it with coordinates via a Wi-Fi connection through an OPC UA server. A SICK LIDAR MRS6000 was used for detecting surroundings attached to a rig holding the LIDAR on the crane trolley and allowing it to move/rotate in a way that surroundings are detected in a satisfying level of precision. Raspberry pi 3 was used for data handling and a PC computer for heavier real time calculations. All parts of the system are connected to the same wireless local area network, except for LIDAR that is connected to the Raspberry Pi with Ethernet cable

Table 1. Hardware capabilities of the overhead crane

<i>Subsystem</i>	<i>Feature</i>	<i>Value</i>
Hoist	Lifting height	3.0 m (6.0 m ^a)
	Lifting motor power	4.5 KW
	Lifting speed	8.00 m/min stepless
	Lifting capacity	3 200 kg
Trolley	Movement range	9.0 m
	Motor power	1.5 KW
	Movement speed	20.0 m/min stepless
Bridge	Movement range	19.8 m
	Movement speed	32 m/min stepless

^a Total rope height, only usable in limited areas.

Main objective was to automate the crane by implementing object collision detection and trajectory planning. To implement that, one fundamental part of the system is the interface between the LIDAR and the crane: Python was used to automatically control the crane's movements whereas the data processing of the LIDAR was done on a standalone C# application. Based on the analyzed LIDAR data, information about the next direction was sent from the C# application to the Python application. The following diagram (Fig. 1) gives a representation of the flow of data from one system to another.

The point cloud obtained from the LIDAR was segregated into grid spaces of 0.5 m by 0.5 m, which was used to map the environment around the crane. Trajectory planning was done using A* based path planning algorithm which took in the current grid position as input and made decision regarding the next grid to move based on two factors: number of point cloud points available in a grid space and the final destination coordinate.

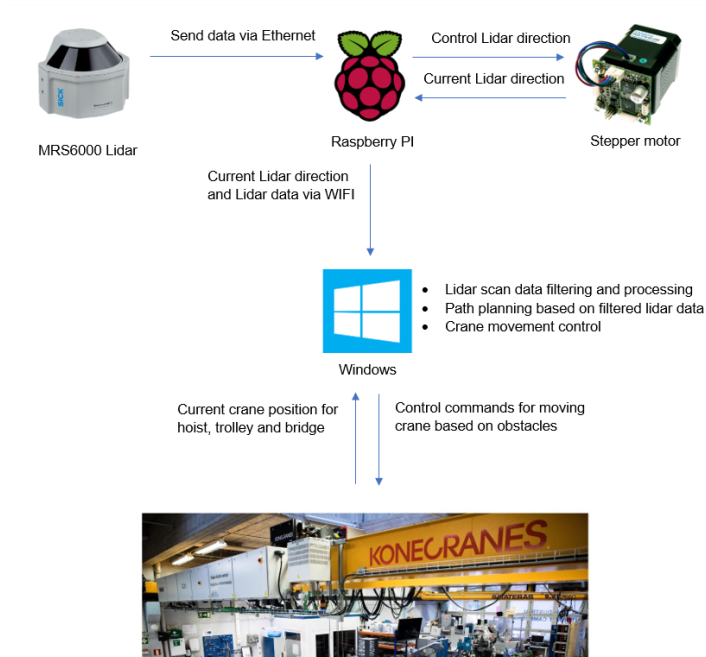


Fig. 1 Data flow in the software side of the crane

For the mounting design of the crane: the LIDAR was placed with its field of view facing downwards and a rotational degree of freedom was given to it to rotate about an axis perpendicular to the ground. The placement of this mounting was done on the trolley so that it could be close to the payload and also obtain power from the trolley.



Fig.2 Rig for placement and rotation of LIDAR

Results

Our final product is a system which comprises of hardware and software components which help in making a LIDAR automated crane system. We have completed a working prototype of an autonomous crane system, which can detect and move an object from a designated pick-up area to a storage area while avoiding obstacles. The working prototype consists of a custom designed attachment to give a 360 field

view to the crane, a software system which analyses the LIDAR data and relays the information to the crane system. The final built system underwent few basic navigational tests in the AIIC warehouse to successfully demonstrate the working of the system.

Discussion

Our system is a proof of feasibility for an intelligent autonomous crane, where it can be integrated into similar systems as the used Konecranes intelligent crane. The LIDAR data is accurate enough to determine common obstacles inside a warehouse such as humans, vehicles, other large machinery, walls and storage shelves. The working area is discretized into grids and as a result, the path planning is dependant on the size of the grids, which needs to be taken into account for future improvements. Human detection could be added in the future for extra safety margins, which could be done either by sensor fusion with the LIDAR and an infrared camera or adding machine learning algorithms for detecting humans. Furthermore, it is possible to develop the system to be fully autonomous as the need for manually fastening the object to the hook can be automated too by using, for instance, a universal gripper.

References:

1. liver Sawodny, Harald Aschemann, Stephan Lahres, An automated gantry crane as a large workspace robot, *Control Engineering Practice*, Volume 10, Issue 12, 2002, Pages 1323-1338, ISSN 0967-0661, [https://doi.org/10.1016/S0967-0661\(02\)00097-7](https://doi.org/10.1016/S0967-0661(02)00097-7). (<http://www.sciencedirect.com/science/article/pii/S0967066102000977>)
2. Sivakumar, P. L., Koshy Varghese, and N. Ramesh Babu. "Automated path planning of cooperative crane lifts using heuristic search." *Journal of computing in civil engineering* 17.3 (2003): 197-207.
3. ShihChung Kang, Eduardo Miranda, Planning and visualization for automated robotic crane erection processes in construction, *Automation in Construction*, Volume 15, Issue 4, 2006, Pages 398-414, ISSN 0926-5805, <https://doi.org/10.1016/j.autcon.2005.06.008>. (<http://www.sciencedirect.com/science/article/pii/S0926580505000713>)
4. Cheng, Tao, and Jochen Teizer. "Modeling tower crane operator visibility to minimize the risk of limited situational awareness." *Journal of Computing in Civil Engineering* 28.3 (2012): 04014004.
5. Cheng, Tao, and Jochen Teizer. "Crane operator visibility of ground operations." *Proceedings of the 28th ISARC* (2011): 699-705.
6. Hrabar, Stefan. "3D path planning and stereo-based obstacle avoidance for rotorcraft UAVs." *Intelligent Robots and Systems, 2008. IROS 2008. IEEE/RSJ International Conference on*. IEEE, 2008.
7. Zhang, Chi & Wang, Junzheng & Li, Jing & Yan, Min. (2017). 2D Map Building and Path Planning Based on LIDAR. 783-787. 10.1109/ICISCE.2017.167.
8. Janson, Lucas, Edward Schmerling, and Marco Pavone. "Monte Carlo motion planning for robot trajectory optimization under uncertainty." *Robotics Research*. Springer, Cham, 2018. 343-361.

9. Kelley, John Joseph, Nathan Eric Bunderson, and Daniel John Morwood. "Path planning system for a work vehicle." U.S. Patent Application No. 15/627,303.
10. Hu, Xuemin, et al. "Dynamic path planning for autonomous driving on various roads with avoidance of static and moving obstacles." *Mechanical Systems and Signal Processing* 100 (2018): 482-500.